Author:
Greenwood, Alexander B

Title:
Characterising Plasmonic Nanostructures with Interferometric Cross Polarised Microscopy

Characterising Plasmonic Nanostructures with Interferometric Cross Polarised Microscopy

Alexander Blake Greenwood

A thesis submitted to the University of Bristol in accordance with the requirements for award of the degree of Doctor of Philosophy in the Faculty of Science, School of Physics.

August 2019

$\sim$ 22,000 words.

Abstract

Plasmonic nanostructures such as gold nanoparticles and nanorods have been the target of many optical studies. Their enhanced optical properties as a result of their plasmonic nature has made them a popular candidate as an alternative to fluorescent markers. Within this thesis interferometric cross polarised microscopy (ICPM), an all optical, confocal like imaging technique is investigated as a means to characterise individual nanostructures. ICPM is first applied to the study of markers used in correlative light electron microscopy. A method that images a fluorescent molecule in light microscopy, and an electron dense gold nanoparticle in electron microscopy, where the two are bound together. Using ICPM it was determined that due to the proximity of the two parts of the probe the fluorescent signal would be significantly quenched, preventing any correlation between the images. Imaging gold nanoparticles with ICPM has often resulted in deviations in the detected scattering signature. It was found that even small variations in a nanoparticles shape is enough to induce extra field components, as a result of their asymmetry. These extra components significantly change the spatial distribution of the detected scattering signature. Through analysis of large arrays of asymmetric nanoparticles, a theoretical model was produced with good agreement with the experimentally collected data. This model is shown to enable a means of detecting the orientation of an individual nanorod in 3D. The same theory was then applied to closely spaced scattering nanostructures, showing that gap sizes as small as 20 nm could be identified. Finally, a chlorine plasma etch method for anisotropic etching of crystalline gold is explored as a method of manufacturing ultra smooth structures, for low loss plasmonic devices, and single photon quantum applications.

Acknowledgements

First and foremost, I would like to thank my supervisor, Dr Henkjan Gersen, for his constant support and guidance throughout the PhD. Whether I was struggling in the lab or in understanding a concept his advice was always appreciated. Thanks to Dr Ben Miles for showing me the ropes during the initial stages of my PhD. Further thanks extend to Dr Krishna Coimbatore Balram for sharing his expertise in nanofabrication and his advice in fabricating the structured samples in this thesis. Sincere thanks also go to Dr Andrew Murray for educating me how to navigate around the cleanroom and the array of processes within.

I would also like to thank Niall Mulkerns, Wil Hoffmann and David Bodey for help proofreading this thesis.

Finally, I would like to thank my parents for their unwavering support throughout.

Author's Declaration

I declare that the work in this dissertation was carried out in accordance with the requirements of the University's *Regulations and Code of Practice for Research Degree Programmes* and that it has not been submitted for any other academic award. Except where indicated by specific reference in the text, the work is the candidate's own work. Work done in collaboration with, or with the assistance of, others, is indicated as such. Any views expressed in the dissertation are those of the author.

SIGNED: ..... DATE:.....

Contents

List of Figures

List of Tables

List of publications

The publications listed below have resulted from the work conducted towards this thesis, and therefore make up a portion of the presented thesis.

1. B. T. Miles, A. B. Greenwood, B. R. Patton and H. Gersen "All-Optical Method for Characterizing Individual Fluorescent Nanodiamonds" ACS Photonics 3, 343–348 (2016)

2. B. T. Miles*, A. B. Greenwood*, D. Benito-Alifonso, H. Tanner, C. M. Galan, P. Verkade and H. Gersen "Direct Evidence of Lack of Colocalisation of Fluorescently Labelled Gold Labels Used in Correlative Light Electron Microscopy" Scientific Reports 7, (2017) [* These authors contributed equally to this work.]

3. A. B. Greenwood, R. Oulton and H. Gersen "Demonstrating the impact of 'real' point sources in spatial mode decomplexing super resolution imaging", **Pre-submission**, (2019)

4. A. B. Greenwood, S. R. Hall, K. C. Balram and H. Gersen "Creating plasmonic devices with atomically smooth side walls through anisotropic etching of crystalline gold", **Pre-submission**, (2019)

Chapter 1

Introduction.

Optical microscopy has found significant usage in the investigation of single cells [1–3]. Markers or labels form a vital component in optical imaging working as a contrast agent specifically targeted at areas or compounds of interest [4,5]. This contrast can for example be generated by fluorescence producing a strong signal at a wavelength that is red shifted from the excitation, or through material properties such as generating a greater scattering amplitude than the surrounding medium. The ability to enable the study of the processes of interest are dependent on the types of marker used; organic fluorescent markers for example are limited to lower exposure times due to bleaching. The motivation behind this work was to further develop an interferometric cross polarised technique focused on the detection and characterisation of the scattering signature from individual nanostructures for their use as biomarkers and beyond.

1.1 Fluorescent Markers

With a wide range of excitation and emission parameters [6, 7] organic fluorophores are the most widely used fluorescent based marker. These fluorophores will absorb light at a specific excitation wavelength, putting an electron in an excited state. The electron does not maintain this excited state for long and will fall to a lower state. This occurs through two different processes; non-radiatively though vibrational losses and radiatively through photon emission. The released photon is of a different wavelength to that used to excite the system caused either by the non-radiative losses, causing a Stokes shift or from two photon excitation [8]. This change in wavelength allows the excited and emitted light to be efficiently separated further enhancing the contrast between marker and background. While these organic fluorophores are small enough to avoid biological interaction and have a wide diversity they are subject to the negative effects of both blinking [9] and bleaching. Blinking is a fluctuation in the emission of the fluorophore as a result of moving to a reversible dark state. Bleaching however is an irreversible transition, permanently preventing fluorescence, often caused by a change in the structure of the fluorophore.

Organic fluorophores are not the only fluorescent probes available; they are joined by a series of nanoparticle based systems such as quantum dots [10–12]. Quantum dots are nanoparticles made from semiconductor materials such as cadmium selenide allowing for the formation of electron hole pairs. The novelty of such particles is their range of fluorescent wavelengths. Adjusting the size of the particles directly affects their excitation and emission properties [10], both being blue shifted by making the particles smaller. One of the largest concerns with using such a particle is their toxicity in biological imaging [12,13]. Non-toxic alternatives such as nitrogen-vacancy doped nanodiamond are also available offering a strong candidate as a non-bleaching, non-blinking, and non-toxic marker [14, 15]. Both these types of particles still have potential issues

with debate over if quantum dots blink or not [16, 17], and the identification of nanodiamonds that express fluorescence [18].

1.2 Plasmonic nanoparticles

Plasmonic nanoparticles, those created from plasmonic materials such as gold and silver, can also be used as a contrast agent [19]. Rather than relying on fluorescence mechanisms, like those mentioned in Section 1.1, the scattering and absorption of these particles can be used to generate a different signal between the particles and the surrounding medium. Signals based on the extinction cross section, the combination of both the absorption and scattering cross section, do not suffer from many of the problems seen from fluorophores such as blinking and bleaching. Plasmonic particles are of particular interest to this scheme of work as a result of their plasmonic resonance [20]. Free electrons in the material can couple to an incident electric field, oscillating at the optical frequency, an effect that is greatest when the field is at the same frequency as the plasmonic resonance of the particle. This resonance generates a dipole, enhancing both the scattering and extinction cross section making their detection easier compared to other non-plasmonic based nanoparticles. This plasmonic resonance wavelength is determined by the size of the particle, for example a gold nanoparticle of 20 nm diameter will have a resonance at around 520 nm [21]. By increasing the size of the particle this resonance is red shifted. The resonance is not only affected by size but also by shape, of which there are many variations. While increasing the size of the nanosphere will shift the wavelength, it requires a large size change to be effective, especially if aiming for the IR region for biological applications. For that reason one of the most utilised from an imaging and medical perspective [22] has been the nanorod.

1.3 Methods of detection

Despite this increase in cross section, the detection of plasmonic nanoparticles through optical means is no easy task. This is a result of the scattering cross section scaling with the diameter to the power of 6 and the absorption to the power of 3 resulting in very weak signals for nanometre-sized particles. A number of different techniques have been implemented for the detection of such particles.

1.3.1 Dark Field

One of the main advantages of using a fluorescent system is the ability to effectively separate out the excitation light from the signal produced, this greatly enhances the signal to background ratio. Scattering particles do not exhibit this same large shift in wavelength, therefore separation from the incident light requires a different methodology. Dark field microscopy achieves this by physically excluding the excitation beam while still collecting the scattered light. There are a number of different implementations of this method though the general principle remains the same. A particle will not only forward scatter, but also scatter light off at an angle. By only detecting light in the areas in which the incident beam can not illuminate, though use of beam blocks and/or using mismatched numerical aperture (NA) objectives, only the scattered light is detected [23,24]. This same principle can be extended to the usage of polarisers to produce a cross polarised detection scheme. Here two orthogonal polarisers are used, the first polarises incident light while the second ensures only light with a modified polarisation can pass. Asymmetric particles with varying optical properties based on which axis is probed, such as the plasmonic nanorods discussed above, can be used in combination with these techniques to enable not only an increased detection sensitivity, but also retrieve their orientation [25].

1.3.2 Photothermal

A power of three dependence for absorption provides a strong advantage over scattering. The plasmonic resonance further enhances the absorption cross section; this parameter can be targeted using a pump probe technique, such as photothermal imaging [26, 27]. In this approach a pump beam is wavelength matched to the absorption peak of the particle, which in the case of a plasmonic particle is its plasmon resonance. Absorption of this probe beam results in the particle generating heat, and as a result, changes the temperature of the surrounding area. This environmental temperature change results in a refractive index change effectively increasing the extinction cross section of the particle. In order to detect a change, a measurement must be conducted both before and after the particle is heated. To achieve this the pump beam can be modulated with some frequency, in turn causing a fluctuation of refractive index at the same frequency. This shifting refractive index can then be detected by a probe beam, and through use of lock-in detection, can be designed to only detect changes occurring at this specific frequency. As the probe beam is not directly detecting the nanoparticle, it can be a wavelength far from the resonance frequency. Enabling separation of both pump and probe beams in a similar manner to fluorescence, with the bonus of enabling the use of high laser powers in the probe beam, to increase the signal to noise ratio. Applying photothermal effects with nanorods provides an added benefit for biological applications as a result of a shifted plasmonic resonance that can be tuned to sit within the biological window [28]. The technique has not only been utilised as an imaging method but also as a cancer treatment [22], where due to the increased temperature surrounding the targeted particles it can be used to selectively kill cancer cells. This does however highlight the disadvantage of the system, to enable high sensitivity high powers are required, which is potentially damaging to biological samples. Such a scheme has been further developed for the detection of single molecules, highlighting the sensitivity that can be achieved [29].

1.3.3 Interferometry

The scattering signal collected for nanoparticles, despite an increased cross section, is very weak. Interferometry can be used as a method to enhance the collected signal [30, 31]. Two paths are followed, often refered to as a signal branch and a reference branch. The combination of these two beams generates interference between them generating two constant terms, that of the signal and reference, and one periodic term, a combination of both terms:

$$\begin{aligned} E(\vec{r},t) &= E(\vec{r},t)_{sig}\, e^{i(\vec{k}\cdot r-\omega t+\phi_1)} + E(\vec{r},t)_{ref}\, e^{i(\vec{k}\cdot r-\omega t+\phi_2)} \\ I(\vec{r},t) &= E(\vec{r},t)^* E(\vec{r},t) \\ &= E(\vec{r},t)^2_{sig} + E(\vec{r},t)^2_{ref} + 2E(\vec{r},t)_{sig}\, E(\vec{r},t)_{ref}\, \cos(\phi_1-\phi_2)\,, \end{aligned} \tag{1.1}$$

where $E(\vec{r},t)$ is the resulting field, $I(\vec{r},t)$ is the intensity, $\vec{k}$ is the wavevector, t is time, ϕ the phase and ω the angular frequency. This periodic signal contains sample information enhanced to a greater intensity by the reference signal. The term further includes details on the phase difference between the two beams enabling further information to be collected if correctly extracted. Further details are presented in Chapter 4. Implementations of interferometric techniques such as Interferometric Scattering Microscopy (iSCAT) have been able to detect individual 5 nm gold nanoparticles [32, 33]. Working in reflection this scheme uses the interface of the sample to generate a signal and reference beam. Part of the beam incident on the surface will be reflected, this makes up the reference signal. Generating the reference in this way gives the benefit of common paths for both beams, making the system less susceptible to environmental fluctuations. The light that passes through the interface will be scattered by any object on the surface, such as a nanoparticle. Scattered light and the reflected reference light is then collected and can be interfered with each other. This implementation enables the 3D tracking of scatterers due to the phase dependence arising from the particles distance from the interface. The reflection scheme

does require some considerations due to its dependence on the interface, such as surface roughness, requiring processing to remove this contribution [34]. The index contrast at the interface will also limit the ability to adjust the strength of the reference, an issue that can be overcome through shaping the NA resulting in the ability to detect individual proteins [33, 35].

An alternative approach to the common path method used by iSCAT is an independent path approach, where a source is split into two paths and interfered after one branch has interacted with the sample. Heterodyne detection can be used with this layout to enhance the desired signal by isolating the periodic signal produced through interference. By imposing a frequency difference between the reference and signal beam, beating frequencies equal to the sum and the difference are generated. Knowledge of this induced frequency can be used in combination with a lock-in amplifier to isolate the difference frequency, further isolating and enhancing the signal. More rigorous details are provided in Chapter 4 Section 2.4.

Heterodyne detection has been implemented in combination with cross polarisation to implement non-linear four wave mixing [36, 37]. In a similar way to photothermal, as described above, four wave mixing uses a pump probe approach. In this instance however two optical pulses are used in combination as a pump and a third as the probe. The two pump pulses excite the plasmon resonance of a gold nanoparticle, the response of which changes its cross section, a change detectable through the probe pulse. This combination is then finally interfered with a reference pulse from the same source. By shifting the frequency of each pulse by some known amount results in the ability to conduct heterodyne detection which, in combination with the crossed polarised scheme, leads to a background free system where a spatial resolution of 140 nm can be achieved.

Laser noise above the shot noise level can hinder the detection limit of a scattering based detection system, overwhelming the desired signal. In this instance balanced detection can be employed [38]. This technique compares the collected signal from two independent detectors as separate entities or a split detector. Any common fluctuations between the two detectors can be removed, such as instability from a laser source. The technique can be directly applied to interferometry, removing the contribution laser power fluctuations from the system, further increasing the sensitivity of the system. This method was utilised by Celebrano *et al.* [39] to achieve single molecule detection through absorption measurements. Scattering approaches have also applied balanced detection to the identification of nanoparticles and viruses in flow, providing options for real time imaging [40].

1.4 Thesis Overview

Focusing on plasmonic particles this introduction has highlighted a number of optical techniques that have been utilised over the years as a means of detecting and imaging plasmonic nanoparticles. Ranging across absorption and scattering methods a number of these techniques have had their resolution pushed, in some cases enabling the imaging of individual proteins. Throughout this thesis, rather than pushing the resolution of interferometric cross polarised microscopy (ICPM), a confocal-like scattering technique, the response to different plasmonic nanostructures is investigated in order to aid in their characterisation. Chapter 2 investigate the usage of ICPM as a characterisation technique for correlative light electron microscopy (CLEM) probes. These probes are designed to enable their detection in both light microscopy through fluorescence and electron microscopy. To enable this an electron dense gold nanoparticle is bound to a florophore. Due to their close proximity reports suggest that this induces quenching of the fluorescence, hindering their usage. Using ICPM to collect the fluorescence and scattering signals these CLEM probes are imaged

to determine if quenching is a potential issue.

Throughout previous experiments discrepencies in the scattering signatures detected by ICPM have been observed. Chapter 3 investigates this phenomenon in more detail studying correlated atomic force microscope images and those from ICPM to identify the cause for these deviations. The implications of such deviations are discussed in relation to spatial mode decomplexing [41], a technique that individually measures the spatial modes as a means of increasing resolution. Shape variation in the imaged nanoparticles was found to lead to deviations in the spatial distribution. To investigate further, large specifically designed arrays of nanostructures were to be imaged requiring the current implementation of ICPM to be modified. Previous iterations of the technique have operated in a transmission configuration requiring a greater number of optical components and limiting the samples to those which are transparent. Chapter 4 describes the building of ICPM to operate in reflection, providing greater stability and the ability to image substrates commonly used in nanofabrication, such as silicon.

Chapter 5 shows the implemented reflection mode imaging a large array of fabricated nanorod structures at different orientations and aspect ratios. From this array of data a model is discussed that begins to explain the scattering signals spatial structure. The model reveals that by appropriate treatment of the collected data that the full 3D orientation of one of these rods could be determined. The model also highlights a distinct difference between two closely spaced scattering structures and a single asymmetric structure. Chapter 6 investigates the transition between these two behaviours to determine if ICPM could be utilised for gap detection in applications such as the nanofabrication used to create the samples throughout this thesis.

Initially these fabrication runs were focused on developing a sample consisting

of crystalline gold, a material well suited for plasmonic structures, due to its lower scattering losses. During development it was found that the material would not etch into the expected structures. Chapter 7 explains that this is a result of an anisotropic etch occurring along the crystalline faces. Chapter 8 then summarises the developments from this thesis and provides an outlook for future development of this work.

Chapter 2

Interferometric Cross Polarised Microscopy for characterising correlative light electron microscopy probes.

Correlative light electron microscopy (CLEM) combines the wide field high speed imaging of light microscopy with the high resolution of scanning electron microscopy. To achieve this a probe visible in both modalities is required to correlate the images. Throughout this chapter a typical CLEM probe is characterised with interferometric cross polarised microscopy. This reveals that the fluorescent part, visible in light microscopy, is quenched by at least 95% by the close proximity of the gold particle, visible in electron microscopy[1].

[1]This chapter contains datasets and analysis from a co-authored paper [42], where I conducted the sample preparation, jointly did the optical experiments, analysis and writing of the manuscript. As well as a second authored published paper [18] where I jointly conducted sample preparation, optical experiments and analysis.

Correlative electron light microscopy (CLEM) is an imaging technique often used in biology as a means of combining the fast wide field imaging of living matter, using light microscopy, with the high resolution of electron microscopy [43]. This combination of imaging systems enables the high resolution imaging of rare events, such as intracellular membrane traffic [44], which would be very difficult to capture using electron microscopy alone. For such a technique to work, a fiducial marker is required in both imaging setups, to be able to align the two images, and ensure that the focus is on the same area. Many of these fiducial markers consist of a fluorophore and a gold nanoparticle [45]; the fluorophore is detectable in light microscopy, and the electron dense gold nanoparticle in electron microscopy. These two are often further bound to a specific biological entity so that the markers can be used to study the biological process of interest [43]. There has however been some doubt about the reliability of such CLEM probes [46–49]. Due to the close proximity of the fluorophore and the gold particle quenching is suspected to prevent fluorescence from the probe, resulting in an unreliable fiducial marker. Within this chapter the use of interferometric crossed polarised microscopy (ICPM) as a means of investigating and characterising a streptavidin labelled Alexa Fluor 633 (Life Technologies/Thermo Fisher) bound to 10 nm gold nanoparticle by Aurion (Wageningen, The Netherlands) will be discussed.

As mentioned previously, CLEM probes are required to provide two signals, one detectable in light microscopy in the form of fluorescence, and the other a high electron density gold nanoparticle that will produce a signal in electron microscopy. A correctly functioning CLEM probe should result in the emitted fluorescence being colocalised with the signature seen in electron microscopy from the gold nanoparticle. In order to test this premise direct correlation between the fluorescence and particle signals is required. We previously combined ICPM with single molecule fluorescence detection as a method to characterise fluorescent 10nm nanodiamond [18]. In that paper the system, as shown in

Figure 2.1(a), was used to ascertain whether the fluorescence produced by the sample originated from NV^- centers within nanodiamonds, or from some form of contamination. Such a characterisation was established by imaging both the fluorescence signal and scattering signal simultaneously and overlaying the results; an example image can be seen in Figure 2.1(b) where the scattering signal and fluorescence signal from nanodiamonds are depicted using a false green and red colour scale, respectively. Figure 2.1(c) and (d) present the linescans depicted in the insert and shows the high localisation accuracy of the system, limited in this image by the pixel size to $\sim$ 50nm.

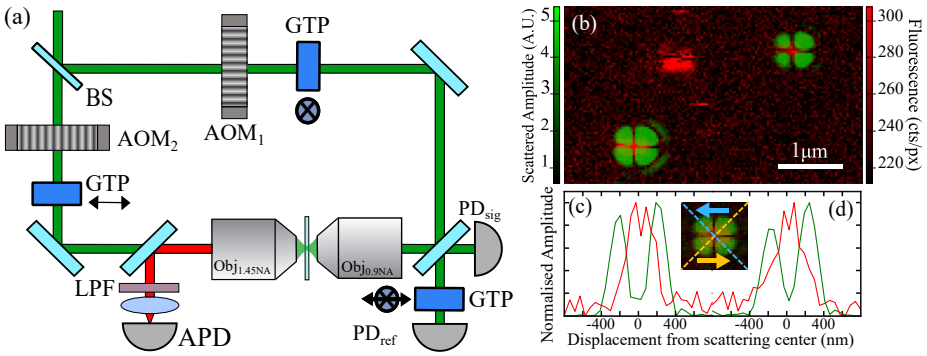

Figure 2.1: (a) Schematic of ICPM in transmission mode with simultaneous single molecule fluorescence detection. Where beam splitters, acousto optic modulators, Glan Thompson Polarisors, long pass filters, photodiodes and avalanche photodiode are represented by BS, AOM, GTP, LPF, PD and APD, respectively. (b) False colour imaging depicting colocalisation as seen in a 10nm fluorescent nanodiamond sample, with green and red representing the scattering and fluorescence signals, respectively. (c) and (d) present the linescans shown in the insert with the direction of the linescan given by the coloured arrows. The fluorescence signal and the scattering signal are shown in red and green respectively.

The primary design and operation principle of ICPM for investigating CLEM probes remains consistant with that of the previous nanodiamond work [18], schematically presented in Figure 2.1(a). In order to collect both the scattering and the fluorescence from single CLEM probes some adaptations had to be made. While the nanodiamonds were excited at 532 nm the Alexa Fluor 633 fluorescent marker on the CLEM probe requires excitation at 633 nm. Not only

does this laser line in our case provide less power in the system but it is also far from the plasmonic resonance of a 10 nm gold nanoparticle. As a result the scattering signal produced at this wavelength provides a worse signal to background ratio. To combat this, two measurements were taken, the first at 633 nm to collect the fluorescence signal, followed by 532 nm for the scattering signal. This order is chosen to prevent bleaching the fluororophores with the increased laser power at 532 nm. Other than incorporating an additional laser source no other system adjustments were made, maintaining the correct overlap by passing both sources through the same single mode fibre, not shown in Figure 2.1. To enable the use of the two different probing wavelengths a notched dichroic (Semrock Di03-R405-R488-R532-R635-t3) was used so that the excitation wavelength can be guided onto the sample while separating the collected fluorescence from the back aperture. To further isolate the fluorescence signal a 635 nm long pass filter (Semrock Di01-R635) is applied before the APD to remove any back reflected excitation light leaking through the dichroic.

Sample preparation was conducted using the following procedure. A glass coverslip (1.5H Marienfeld) underwent a 10 minute submersion in a two parts nitric acid and one part sulphuric acid solution followed by two 10 minute submersions in deionised water, and dried with a nitrogen spray gun. 50 μL of stock CLEM probe solution is then drop deposited onto the coverslip before excess is removed by a nitrogen spray gun after two minutes.

Figure 2.2(a) presents the result of imaging the CLEM probes as received, which is how these probes are typically used in CLEM experiments (Verkade, P. (2017), personal communication), with the scattering in green and fluorescence in red. The disparity between fluorescence and scattering signatures is immediately apparent, showing that there is a significant difference between the number of gold nanoparticles and Alexa Fluor 633 fluorophores. This clearly demonstrates that the initial sample contains a significant fraction of unbound fluorophores. The

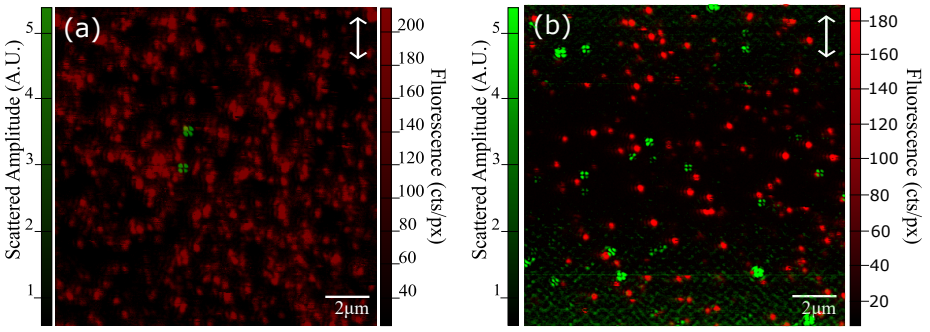

Figure 2.2: (a) False colour image of as received CLEM probes and (b) after purification through centrifugation, with green and red representing the scattering collected with ICPM and fluorescence from the APD, respectively. Both images are 23.2 μm x 25.0 μm with 512 pixels x 512 pixels at a scan rate of 0.78 ms/px. The incident polarisation is depicted by the arrow in the top right.

exact ratio between scattering particles and fluorophores is difficult to determine given the high density of fluorescence signatures hindering the identification of single fluorescent spots. Diluting the sample to lower the amount of fluorescent signatures would result in a significant reduction of scattering particles, maintaining the difficulty in identifying the ratio between the two. Despite the considerable number of fluorescence signals there is no identifiable colocalisation between any of the fluorescence signals and the scattering signature. To investigate these probes further and to identify the root cause for the lack of colocalisation a greater number of scattering particles would be required for statistical analysis. Using the mass difference between the two constituents in the solution, centrifugation can be used as a means of separation. The sample solution was therefore centrifuged at 15,700g for 20 minutes. The supernatant, containing many of the free fluorophores, was disposed of before the addition of 200 μl of deionized water. The sample was then sonicated for 20 minutes so as to re-disperse the separated material. This process was repeated three times. While this method will still result in some free fluorophores in the final sample this significantly increases the ratio between bound and un-bound Alexa Fluor 633 as can be seen in Figure 2.2(b). The inherent nature of centrifugation has potential for the CLEM probes to aggregate during the purification process. To

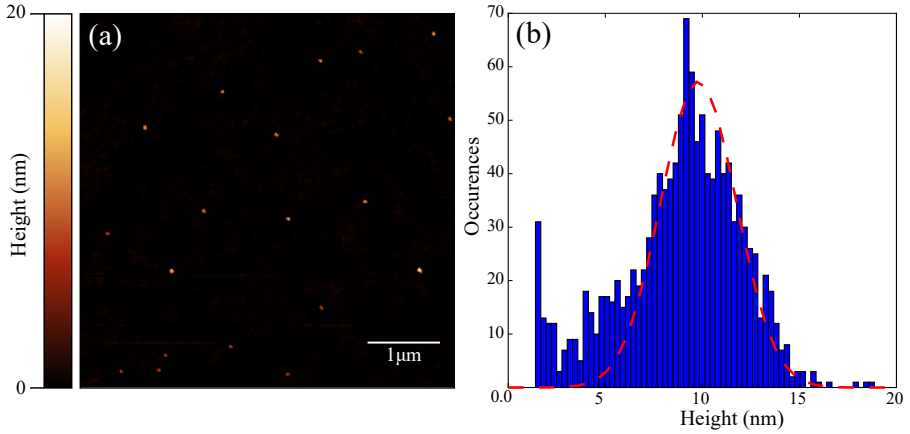

Figure 2.3: (a) AFM image of deposited CLEM probe after purification, taken at 9.8 nm/px in tapping mode. (b) A histogram showing the height distribution of 1,258 particles. The red dotted line shows a Gaussian fit with a FWHM of 4.6nm.

alleviate this concern a sample was prepared, in the same manner, and analysed through the use of atomic force microscopy (AFM), the results of which can be seen in Figure 2.3. The AFM image in Figure 2.3(a) shows that the sample is monodisperse with no sign of particle aggregation and that there is sufficient particle spacing to allow for imaging individual CLEM probes with a diffraction limited approach. Figure 2.3(b) presents the gold nanoparticles size distribution as seen in 14 randomly selected areas in which a total of 1,258 particles were imaged. The data is fitted with a Gaussian fit revealing a mean particle diameter of 9.8 nm $\pm$ 2.3 nm as determined from the FWHM.

Figure 2.4 presents fluorescent images of a typical area of the purified sample studied under two orthogonal polarisations, as depicted by the arrow in the top right. The images are taken sequentially, rotating the GTP 90^{o} after the first image. The effect of the polarisation on the fluorescent signal can be seen by comparing Figure 2.4(a) and (b). As expected with fluorescence imaging with a high NA objective the fluorescence signature is slightly elongated along the polarisation direction. Figure 2.4 also provides evidence for single molecule detection by the system as demonstrated by the fluorescence signal in the an-

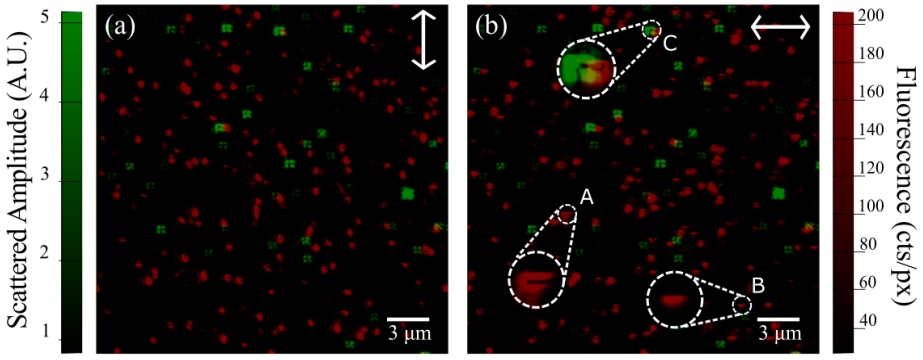

Figure 2.4: False colour image of purified CLEM probes with green and red representing the scattering and fluorescence, respectively. The arrow in the top right depicts the incident polarisation direction. Annotations *A*, *B* and *C* highlight evidence of blinking, bleaching and fluorescence signals in close proximity to scattering signals. Images are collected at 0.78 ms/px with an image size of 23.3 μm x 25.0 μm at 512 pixels x 512 pixels. 14.9 μW are used at a wavelength of 532 nm for scattering signal and 7 μW at a wavelength of 632 nm for the fluorescence signal.

notated boxes A and B. A shows a typical example of blinking behaviour, the fluctuation in fluorescence intensity resulting from an excursion to the triplet state, as seen by the black line through the fluorescence signature. Whereas B depicts evidence for discrete bleaching, a permanent change to the molecule preventing it from fluorescing, as seen by the sudden disappearance of signal during the imaging scan leaving a fluorescent signature that looks incomplete. Both indicate that a single molecule is being probed as it is unlikely that two close molecules would be affected in the same fashion simultaneously. The observed scattering signatures resemble the form of the expected clover-leaf distribution from ICPM. Due to the relatively large distribution of intensity between the numerous scattering particles the colour scale is clipped to ensure that all scatterers are visible. This does result in a distorted cloverleaf image for a number of the scatterers but doing so still enables clear identification of the presence of a scattering particle and the location of its centre. While there are several instances of a fluorescent signal close to a scattering signature, similar to that seen in annotated box C, there are none that fully colocalise as was seen in Figure 2.1(b) for NV^- centres in nanodiamond. It can also be seen that these

close fluorescent signals are not offset in a constant direction across the sample in each instance disputing an argument for a potential misalignment between the two channels.

To enable a statistical study the collected images were processed so as to provide the maximum photon count for a given fluorescent signature with each fluorescent signature being identified by a local maximum above 20 cts/px for both polarisation images. The fluorescence signatures collected for one polarisation were then compared to that of the orthogonal polarisation, so that pairs of fluorescence signatures were obtained.

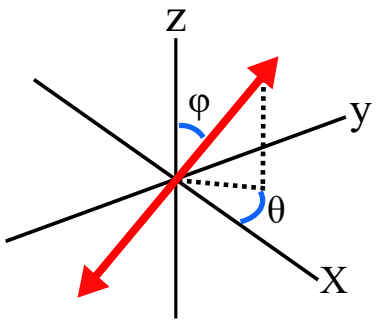

Figure 2.5: Diagram depicting the angles used to describe the dipole orientation in Equations 2.1 - 2.3

Due to the dipole nature of the fluorophores their fluorescence signal is dependent on the incident polarisation which must be considered throughout the imaging process. Should a dipole be oriented perpendicular to the incident polarisation there would be no fluorescent signal. To negate this influence of the in plane angle, imaging using two orthogonal polarisations or using circularly polarised light is required. This ensures that there will always be a detectable fluorescence signal independent of the dipoles orientation. Due to the polarisation components available, two orthogonal linear polarisations are used for imaging. The collected signal from these two polarisations can then be combined to provide a fluorescence value independent of the in-plane angle [48]. Given

a dipole moment ρ for an arbitrarily orientated fluorophore with a linearly polarised incident electric field, E_α, where α represents the axis of polarisation, the resulting fluorescence signal, K_α, can be written as:

$$K_x = \sum_{i=1}^{N} \mid E_x \, \rho_i \, sin(\phi_i) \, cos(\theta_i) \mid^2 \tag{2.1}$$

$$K_y = \sum_{i=1}^{N} \mid E_y \, \rho_i \, sin(\phi_i) \, sin(\theta_i) \mid^2 , \tag{2.2}$$

where θ_i and ϕ_i are the Euler angles used to describe the orientation of the ith dipole, as defined in Figure 2.5. The summation is to average all fluorescent signatures in the whole image, where N is the number of dipole emitters. The combination of these two values results in a fluorescent signal that is only reliant on the out of plane angle, K_{xy}:

$$K_{xy} = K_x + K_y = \sum_{i=1}^{N} \mid E\rho_i \sin(\phi_i) \mid^2, \tag{2.3}$$

The fluorescent pairs were identified by looking for fluorescence signatures within an arbitrary distance of each other, in this instance 0.17 μm. While the matching of scattering signals in both polarisations is used to account for any spatial shift the 0.17 μm range accounts for any error in this process, ensuring only the maxima's location is paired. The average photon count per pixel for a circle of radius 0.17 μm is then established as the fluorescent signal for that area. This method ensures that the fluorescence in question has been imaged using both polarisations enabling K_x and K_y, as defined in Equation 1 and 2, to be established. There by allowing the calculation of K_{xy}.

By also establishing the background fluorescence, through pixel values further than 0.17 μm from a fluorescence or scattering signature, it is possible to then determine not only if there is colocalisation between the two signals but also to what degree the fluorophore is quenched by the proximity of the nanoparticle. Figure 2.6 presents histograms for these values: (a) background photon

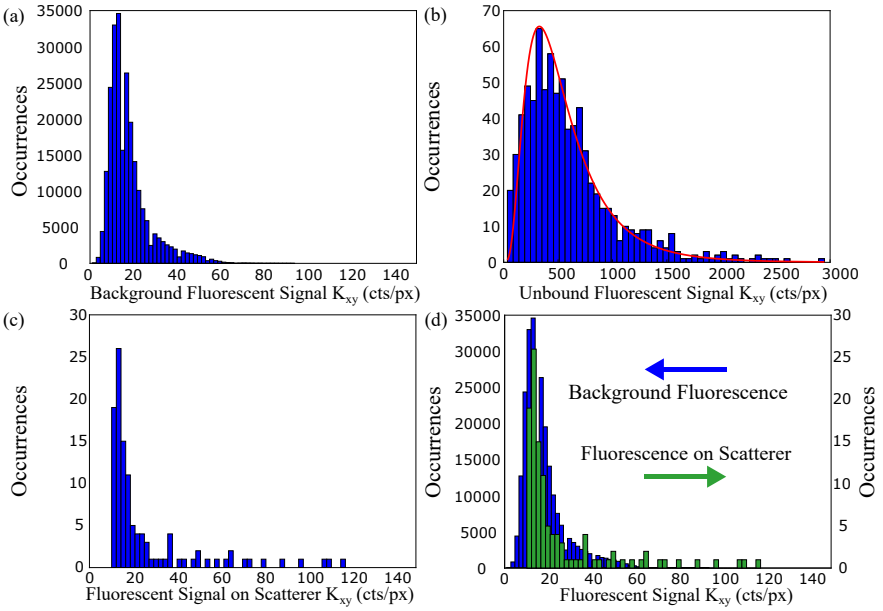

Figure 2.6: Histograms depicting the average photon count per pixel for each fluorophore in the three fluorescent situations. (a) The background fluorescence count from the sample. (b) The fluorescent count produced by fluorophores not associated with a scattering particle with a lognormal distribution fitted in red. (c) The fluorescent count at the centre of a scattering signature. (d) Overlays the histograms from (a) and (c) to highlight their distinct similarity.

count, (b) fluorophore photon count, and (c) photon count on a scattering signature. Each histogram has a clearly defined peak with the unbound fluorophores showing a strong lognormal distribution, as is expected [50]. For the fluorescence signal related to the scattering particles the histograms peak is at a count of 17.5 cts/px, marginally higher than the background value of 17 cts/px yet significantly lower than the 328 cts/px for the signal from fluorophores not in proximity of a scattering signature. Overlap of the background fluorescence and fluorescence on scatterer histograms can be seen in Figure 2.6(d). While there is a long tail in Figure 2.6(c) that indicates that some do experience a higher fluorescence signal, closer inspection of these individual points show that the longer tail is caused by an unbound fluorophore with its location just outside the 0.17 μm but close enough that some of the spot is still collected. This analysis therefore establishes that either no scattering particle is bound to a fluorophore

or that the proximity of the gold particle to the Alexa Flour 633 quenches it by over 95%, the amount required to decrease the fluorescence to background levels. To confirm the attachment of the fluorophore, diffusion-ordered spectroscopy NMR (DOSY) was conducted on the CLEM probe, seen in Figure 2.7. This technique correlates the size of the structure, through diffusion, with an NMR spectrum. The red box highlights that the majority of the sample shares the same low diffusion constant an indicator of a large structure, confirming the binding of the Alexa Fluor 633 to the gold nanoparticle. Some molecules in the solution do not share the same diffusion coefficient however this is seen to be contamination in the sample such as the citrate, highlighted in green.

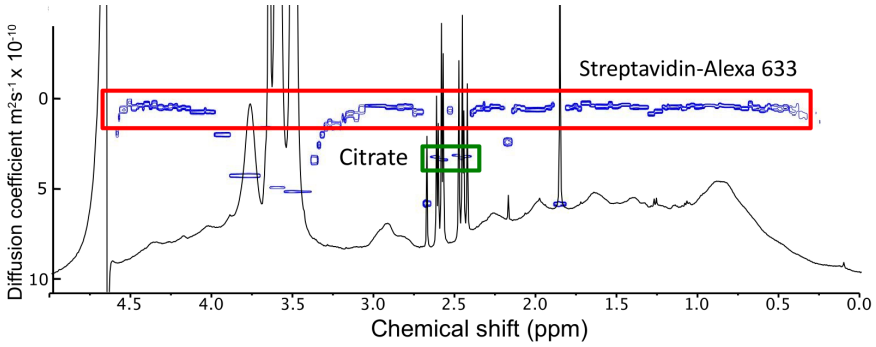

Figure 2.7: Overlayed H NMR, black, with DOSY, Blue. Streptavidin and Alexa Fluor 633 are shown to share a low diffusion coefficient indicating their binding. A citrate signature is highlighted as an example of extra molecules that do not share the same diffusion coefficient. Data collected by David Benito-Alifonso [42].

Within this chapter the effectiveness of an example CLEM probe, 10 nm gold nanoparticle bound to streptavidin labelled with Alexa Fluor 633, as a fiducial marker was investigated. Through investigating the fluorescence signal that arises from the same location as scattering signatures and comparing this value to that seen from fluorophores that are well separated from scattering signatures it was found that the proximity of the gold nanoparticle to the fluorophore results in a fluorescence quenching of over 95%. It was also found that the initial stock solution contained a very high number of free fluorophores. These results

highlight the importance of characterisation studies on such CLEM probes at the single particle level.

Chapter 3

Demonstrating the impact of "real" point sources in spatial mode dependent imaging.

Optical microscopy is ever driven by the desire to push resolutions past the diffraction limit. In this chapter the influence of real point-like particles on the generated modal components are investigated and how this could be an issue for new quantum inspired super-resolution techniques relying on modal decomposition[1].

[1]This chapter contains datasets and analysis from a manuscript being prepared for submission

Imaging identical point-sources separated by distances less than the diffraction limit is a fundamental, yet complex problem in optics. This challenge has in the past been addressed in many ways including by approaches such as near field imaging [51], saturated scattering [52, 53], localisation microscopy [54–56] and structured illumination [57,58]. Inspired by quantum mechanic approaches there has recently been a paradigm shift to tackle this challenge arising from the realisation that collection and processing of the full electromagnetic field contains extra information through the phase that can be exploited. One way this concept has been demonstrated for imaging is through spatial mode demultiplexing (SPADE) [41], in which the amplitude of each individual Hermite Gaussian mode scattered by the point sources is collected, conceptually depicted in Figure 3.1. By looking at the full modal make up of the collected signal it is predicted to be possible to avoid the limitations imposed by diffraction [59]. This concept has been explored practically in a number of different schemes with low numerical aperture (NA) lenses [59–61]. However to date, to the best of our knowledge, this has not been implemented with high NA objectives commonly used to image biological samples with higher resolution. Intriguingly these high NA objectives, used in biological and fluorescence imaging, generate distinct spatial modes at the focus resulting from strong focusing [62]. Conceptually, one of these spatial modes can be selected and utilised in a similar way to that of binary SPADE [41]: a simplified version of SPADE that separates only the TEM_{00} mode from all others through the use of an appropriate local oscillator. This use of a single mode does however come at a cost of decreasing the Fisher information for an increasing separation of the two point sources [60]. Here this approach for high NA objectives by imaging identical real point-sources separated by less than the diffraction limit is experimentally demonstrated. By correlating images of closely spaced 60 nm gold nanoparticles from our interferometric optical approach with those from atomic force microscopy (AFM) the importance of considering any deviation from the "ideal" point source on the detected signal is demonstrated.

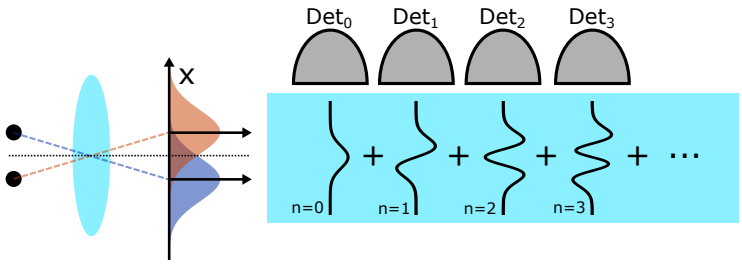

Figure 3.1: SPADE concept diagram based on the work of Tsang *et.al.* [41] depicting two point sources imaged with a single lens to produce a combined image. In Tsang's work the full information is collected in a fibre and each individual mode is selectively coupled out for individual detectors. This could be achieved through specifically selected single mode fibres or use of a grating.

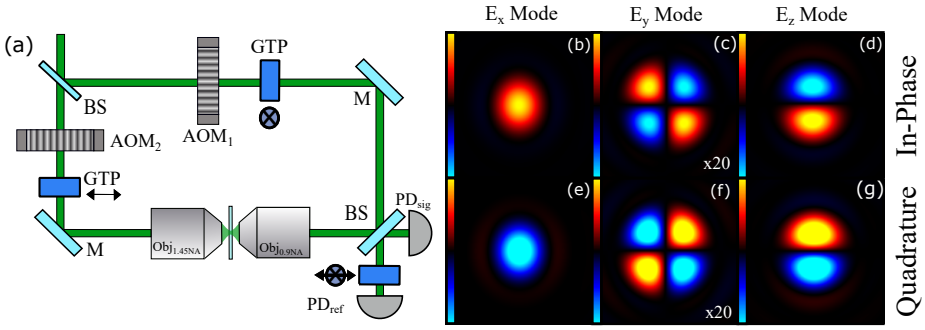

Figure 3.2: (a) Schematic of the high NA interferometric imaging system where mirrors, beam splitters, acousto optical modulators, Glan Thompson Polarisers, photodiodes and objectives are denoted by M, BS, AOM_i, GTP, PD_i and Obj respectively. (b), (c) and (d) show the in-phase part of the generated spatial modes, generated by a high NA objective. With (e), (g) and (f) depicting the corresponding quadrature parts of the spatial distribution. (c) and (f) are scaled due to the intensity difference between modes, as denoted in the bottom right corner.

A diagram of the optical system used is shown in Figure 3.2(a). At the focus of a high NA objective, such as the 1.45 NA objective used here, three different spatial modes are present for the different field components in the focus, resembling the TEM_{00}, TEM_{11} and TEM_{01} modes for E_x, E_y and E_z, respectively. The in-phase component of these modes are shown in Figure 3.2 (b) - (d) with the quadrature component in (e) - (g), respectively, with further details found in Chapter 4.2. In contrast to binary SPADE each individual spatial mode here

has a distinct polarisation state. By selecting a frequency shifted local oscillator that matches the polarisation state of one of these modes, such as the y -polarised mode in Figure 3.2(c) and (f), it is possible to image a sample using only the selected spatial mode, while collecting both the amplitude and phase of the light scattered by the point sources. This TEM_{11} like mode is selected as it provides an advantage to resolving closely spaced point particles due to the phase structure of this y-polarised mode enabling greater signal for off axis particles. To compensate for the difference in strength of the different spatial modes acousto optic modulators are used to enable frequency based heterodyne detection to enhance the signal to background of the desired mode.

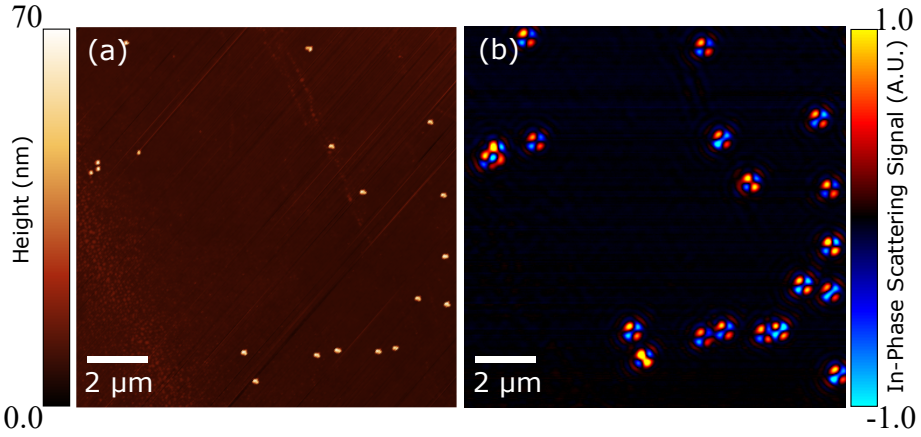

Figure 3.3: Correlation of 60 nm gold particles between AFM, (a) and the presented optical scheme, (b). The AFM image has been rotated for easier identification of particles in both images and shows that relocation of individual nanoparticles is possible for a direct comparison between imaging techniques.

In order to study the response of closely spaced point sources and characterise any resolution enhancements 60 nm gold nanoparticles were imaged. Gold nanoparticles were selected here due to their high scattering cross section at resonance and point-like particle nature, simplifying the response of the system. To convincingly demonstrate any resolution enhancement, the sample under study needs to be compatible with both the optical scheme and an imaging system with far greater resolution. While scanning electron microscopy (SEM)

is often used for the imaging of gold nanoparticles, the requirement of conductive samples limits the potential substrate choice. AFM does not have this limitation and has a resolution significantly greater than the optical diffraction limit. However to be able to fully characterise the sample the same location needs to be imaged in both these imaging approaches. Both the optical and AFM systems used here include bright field cameras, so that relocation can be achieved through the fabrication of a gridded overlay to act as a fiducial marker. Therefore a Cr/Au grid was fabricated through photolithography and thermal evaporation on a glass cover slip (Marienfeld 1.5H) as a substrate, enabling transmission based measurements. An AFM image of the fabricated sample is shown in Figure 3.3(a), depicting a range of particle separations. Figure 3.3(b) presents the same area imaged using the interferometric optical scheme presented in Figure 3.2(a) and demonstrates the ability to relocate and image the same particles in both techniques. To demonstrate the strong dependence of the optical signal on particle separation Figure 3.4 presents data sets for the instance of one, two and three particles. Figure 3.4(a) - (c) shows these situations under AFM with (d) - (f) displaying the collected in-phase scattering signal imaged with the E_y mode and (g) - (i) showing the quadrature part. This result clearly shows that there is a distinct difference in the collected pattern for multiple closely spaced particles compared to the instance of a single particle.

On closer inspection Figure 3.4(d) and (g) reveals a deviation from the expected spatial distribution for a single scatterer. As seen in Figure 3.4(a) the collected signal comes from a single particle yet does not produce the expected spatial mode seen in Figure 3.2(c) and (f). The imaging mode contains a central zero along the x and y axis, which is not present in the collected image. This unexpected behaviour is highlighted in more detail in Figure 3.5, where several individual particles and their AFM image have been presented.

All of the example particles in Figure 3.5 were part of a single image from each

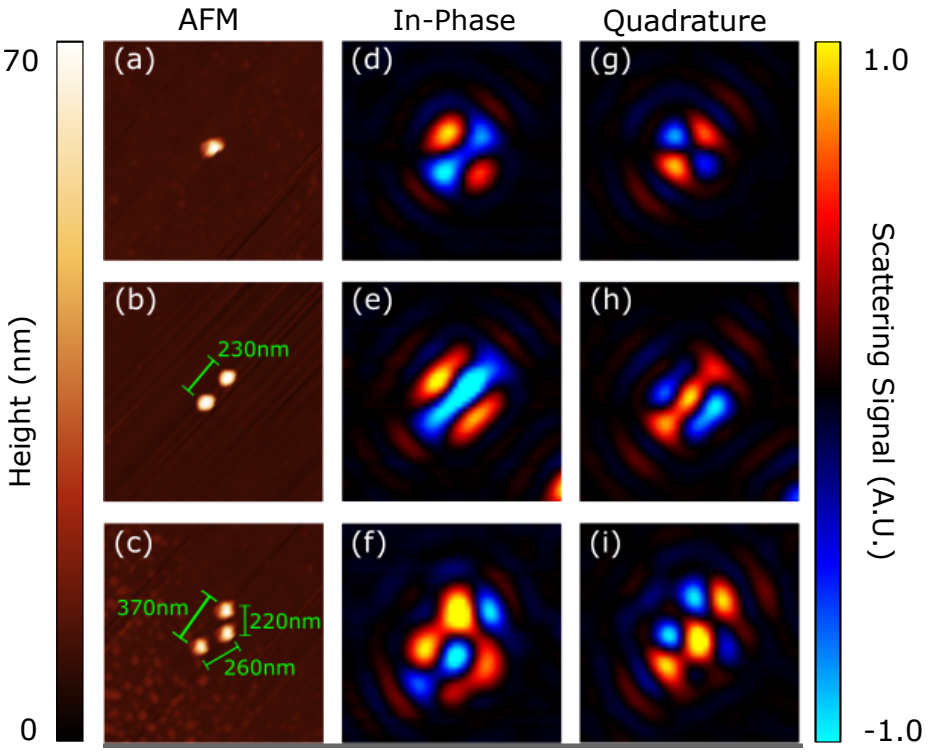

Figure 3.4: (a) - (c) show AFM images of individual, pair and triplet 60 nm gold nanoparticles spaced below the diffraction limit. (d) - (i) show the scattering signal of these same particles imaged with the generated E_y mode where (d) - (f) present the in-phase component and (g) - (i) the quadrature component. The merging of the spatial patterns in the case of the multiple particles are clearly seen and the increasing complexity of the spatial structure when multiple particles are involved. Each image is 1.2 μm x 1.2 μm.

imaging system eliminating changes in AFM tip shape. The degree of variation between scattering signatures within a single image may suggest that drift in the system could be the cause. The drift of this system was previously investigated [63], it was found that over 3.5 hours there was a $0.41\mu m \pm 0.04\mu m$ displacement of the spatial structure. Given that an individual image is collected in $\sim$ 8.5 minutes the drift is likely to be minor, estimated at less than 0.02 μm per scan. While the drift may only cause small displacements it would potentially still result in an uneven overlap of the local oscillator and the collected signal. The resulting change in overlap accuracy between the two beams could potentially generate asymmetric spatial signature. However to demon-

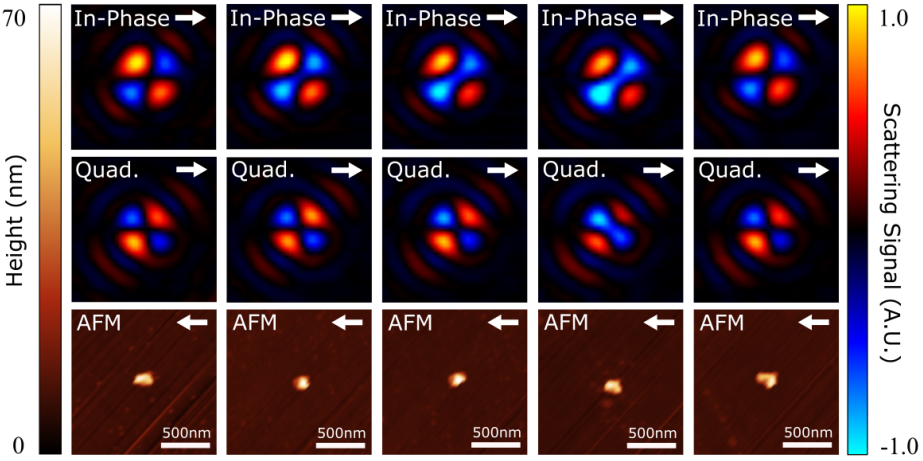

Figure 3.5: A selection of individual nanoparticles selected from a single sample imaged both optically, with In-Phase and Quadrature parts in rows one and two respectively, and AFM (bottom) highlighting how the variation of particle shape can affect the scattering signature produced to the extent that expected zeros are not present in the centre of the spatial distribution.

strate that the combination of these two spatial distributions would not be capable of reproducing the structures depicted in Figure 3.5; drift in the spatial distribution is simulated for small variations in the off axis angle of the signal beam, as is depicted in Figure 3.6(a). This was carried out by summing the local oscillator and signal fields with different offset central positions, as represented by d in Figure 3.6(a) with the results shown in Figure 3.6(b) - (e). This results in different lobes to be enhanced. This enhancement cannot result in a signal between these lobes as seen throughout Figure 3.5.

The obtained images can in fact only be understood by realizing that the E_x and E_z modes, shown in Figure 3.2(b) and (d), respectively, are also present in the final spatial structure. Arbitrary examples of these structures can be seen in Figure 3.7(a) - (d) where varying degrees of each mode are mixed onto the expected isolated E_y mode. The simulations used to generate these modes is based on the mathematical description from Novotny and Hecht [64]. Varying the strength of these additional modes enables the detected spatial distribution for a single particle to be reproduced, as shown in Figure 3.7(e) - (h). The π

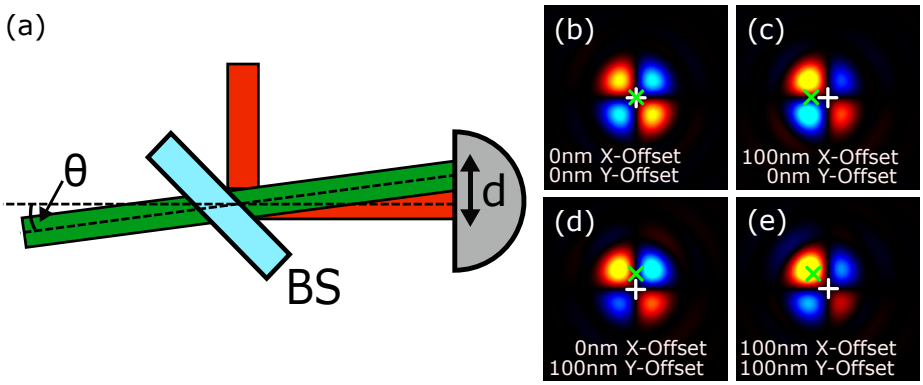

Figure 3.6: (a) Schematic diagram of the overlap between the local oscillator (red) and the signal beam (green) where BS is the beam splitter and θ is the small off axis angle that results in an overlap shift d. (b)-(e) simulate various overlaps of the reference and signal beams resulting in a varying spatial structure. Insert in each image provides information for each of the offsets parameters.

phase difference seen between the images in Figure 3.7(a) - (d) and Figure 3.7(e) - (f) is a result of the phase reference used while collecting the experimental data.

The AFM images shown in Figure 3.5 also show a varying shape of the individual particles throughout the single image. It is unlikely that the tip convolution is going to vary at each particle, suggesting that particles differ in shape, as has been identified in other works [37]. The variation in the spatial distribution between collected signals is therefore likely to arise as a result of these real particles not being true point particles, in effect breaking the symmetry of the system. A variation in shape would cause the particle to be asymmetric along different axis. Such asymmetry is clearly having a significant effect on the resulting scattered light. This effect can be understood from the fact that asymmetry in the scattering structure projects polarised light onto other axis; in a similar manner to a polariser at 45° to an incident linearly x polarised beam will project equal amounts on to the x and y axis. In this optical interferometric scheme this results in a variation in the scattering signature due to the different polarisation modes contributing to the final scattering signature. This polarisation projection is caused by the symmetry breaking structures of

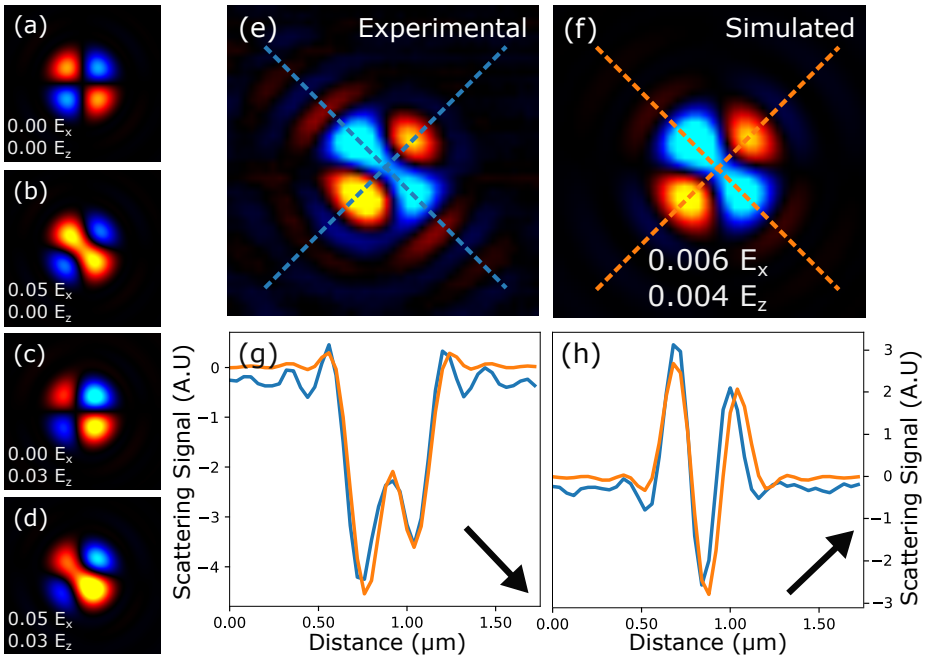

Figure 3.7: (a)-(d) Simulated scattering signature produced when including different strengths of extra field components generated by a high NA objective. (e) Experimentally collected scattering signal from single nanoparticle. (f) Spatial distribution simulated to match (e) through variation of the amplitude for the contributing spatial modes. (g) and (h) compare the line scans from both experimental (blue) and simulated (orange). (g) shows bottom to top diagonal and (h) top to bottom diagonal, as depicted by the inserted arrows.

real particles compared to that of theoretical point particles, a property that has implications for other optical systems.

The imaging of 60 nm gold nanoparticles both optically and through AFM has revealed that they cannot be treated as ideal point particles, as has been the case for other sizes of gold nanoparticles [65]. This non-ideal nature has a dramatic influence on the concept of using the generated modes for super resolution imaging. The combination of multiple modes in the isolated signal from an individual asymmetric point source significantly influences the ability of the system to spatially resolve point particles in real applications. The separation of closely spaced particles through systems such as SPADE rely on the asymmetric modes generated from only that pair. Should the collected signal also contain the extra

modes generated from non-ideal point particles then separation becomes significantly more difficult or potentially impossible. In essence with both asymmetry in individual particles and particle pairs generating extra modal components the separation and characterisation of the full situation requires a method of determining the model contribution from each source, not just the overall structure.

While 60 nm are considered fairly large for the use of biological applications and are also more likely to be affected by surface irregularities, evidence of these effects has been seen with 30 nm particles with an asymmetry of only 0.5% and will also occur for smaller particles due to the crystal structure [37]. This effect of realistic point sources projecting into different spatial modes not only affects scattering effects. In fact this phenomena has the potential to also influence any dipole emitters, such as the single fluorophores often used in biological applications as they have a different spatial distribution depending on their orientation [66].

Chapter 4

Implementation of Interferometric Cross Polarised Microscopy in Reflection.

Interferometric cross polarised microscopy (ICPM) has in the past been configured to work in transmission. This approach is not ideally suited for the imaging of large arrays of fabricated nanostructures. To increase stability, ease of use and allow a wider variety of sample types, ICPM was rebuilt to function in reflection. This chapter describes the system and its operation in reflection.

4.1 Motivation

Interferometric imaging plays a crucial role in many applications, including astronomy [67, 68], nanofabrication [69, 70] and to resolve features in biological samples without labelling [71, 72]. Interferometric cross polarised microscopy (ICPM) is one implementation of such an interferometric technique, as discussed in Chapter 2. The demonstrated implementation of this scheme to date relies on forward scattering, which places a number of restrictions on the samples that can be imaged. Implementing the technique in reflection, as has been done with similar systems [37], would alleviate many of the problems associated with a forward scattering system. Biological samples are often made up of highly scattering, heterogeneous material and in many cases, unless sectioned, have a significant thickness [73]. This combination of properties results in a sample that is difficult to image in transmission, especially with a technique reliant on polarisation. By transitioning the technique to work in reflection the requirement to collect light that has passed through a sizeable scattering medium is removed, increasing the imaging capabilities of the system. Moreover with a single objective for both illumination and collection the number of optical components can be reduced, significantly reducing costs and alignment complexity while increasing stability. Further advantages of a reflection based system over transmission can be found in the ability to image on non-transparent samples, as are many of those used in nanofabrication, such as silicon. The increased stability is an important factor in interferometric techniques as a result of phase shifts with a varying sample position. This enables a greater area to be scanned without realignment of the system, ideal for the characterisation of nanofabricated structures. Here the building and investigation into the implementation of ICPM in reflection mode for the application of imaging a large array of nanofabricated structures is described.

4.2 Functional overview/operating principle

Here an overview of the operating principles and data collection methods are discussed. The system makes use of a number of noise/background reduction techniques including cross polarisation, interferometry and heterodyne detection.

4.2.1 Crossed Polarisation

When polarised light is focused by a high numerical aperture (NA) objective components are projected onto all three planes X, Y and Z, as well established since Richards and Wolf [62]. Objects in the focus scatter these components to the far field which are then collected by the same focusing objective. By passing the collected light through a polariser orientated orthogonal to the incident beam the excitation light can in principle be completely removed, assuming an infinite extinction ratio. The remaining light is only the light that was scattered by an object within the focus. In principle this enables background free detection due to a major contribution to the background signal being removed. In practice however there are still several limiting factors: detector noise and sensitivity, the finite extinction ratio of polarisers, the low proportion of light that is shifted to the orthogonal polarisation, and the generated Maltese cross [**?**]. The contribution from the latter is removed through overlap of a Gaussian reference and integration though a point detector, resulting in the out of phase lobes to cancel [74]. Further to removing the influence of the Maltese cross, Wilson and Tan showed that this technique also addresses the finite extinction ratio, highlighting that the extinction will always be infinite when using the Gaussian reference [75].

4.2.2 Imaging Objective

The role of the NA in microscopy is an important one as it is directly related to the achievable resolution, as seen in Abbe's diffraction limit, expressed by:

$$d = \frac{\lambda}{2n\,sin(\theta)} = \frac{\lambda}{2NA}\,, \tag{4.1}$$

where d is the minimum resolvable distance, θ is half the angle of the light cone from the lens, n is the refractive index and λ represents the imaging wavelength. Equation 4.1 also provides a mathematical definition of the NA. In essence it is a measure of the angles over which light can be collected by an objective. Higher NAs allow a greater collection of light, which has led to their heavy usage in single molecule fluorescence experiments as it allows for the collection of more signal [76]. This extra signal collection is also a strong contributing factor to the desire to use a 1.45 NA objective in this experiment. For ICPM the NA has additional influence as a result of its reliance on the E-field components generated in the focus [77]. A higher NA generates a greater proportion of the component polarised along the y-axis relative to the one along the x-axis, leading to an increased signal interfering with the orthogonally polarised reference.

4.2.3 Interferometric Enhancement

To address the low signal levels and overcome detector noise the collected signal (E_{sig}) is enhanced through interference with a reference beam (E_{ref}) of a parallel polarisation. Implementing this using a separate branch enables us to remain independent of the excitation component, which is crucial to work on photosensitive samples, such as the experiments conducted in Chapter 2. This can be written as;

$$E(\vec{r},t) = E_{sig}(\vec{r},t)e^{i(\vec{k}\cdot r-\omega t+\phi_1)} + E_{ref}(\vec{r},t)e^{i(\vec{k}\cdot r-\omega t+\phi_2)}\,, \tag{4.2}$$

where $E(\vec{r},t)$ is the resulting field, $\vec{k}$ is the wavevector, t is time, ϕ the phase and ω the angular frequency. For the detection of the combined optical signal

we can only observe the intensity due to the high frequencies of optical signals.

$$\begin{aligned} I_{\vec{r},t} &= E^*_{\vec{r},t} E_{\vec{r},t} = E^2_{sig} + E^2_{ref} + E_{sig}E_{ref}(e^{i(\phi_1-\phi_2)} + e^{i(\phi_2-\phi_1)}) \\ &= E^2_{sig} + E^2_{ref} + 2E_{sig}E_{ref}\cos(\phi_1 - \phi_2) \end{aligned} \tag{4.3}$$

From this equation we can see that even if E_{sig} is very small it can be enhanced by interference with a suitable reference signal. This still detects the $E^2_{sig}+E^2_{ref}$ component in which E^2_{ref} dominates the noise. To extract the signal the periodic nature of the desired signal component can be utilised.

4.2.4 Heterodyne detection

To further reduce the background heterodyne detection is employed to remove the noise resulting from the E^2_{ref} term as well as move away from low frequency noise in the electronics [78]. The reference and signal branch undergo a frequency shift ($\Delta\omega$) relative to each other. When the two interfere a beating frequency, equal to the difference in frequency, is generated, given by:

$$E^2_{sig} + E^2_{ref} + 2E_{sig}E_{ref}\cos(\Delta\omega t + \Delta\phi)\,, \tag{4.4}$$

where $\Delta\omega$ and $\Delta\phi$ are the shift in angular frequency and phase difference, $\phi_1 - \phi_2$, respectively. From this signal E_{sig} can be retrieved by multiplying the signal detected with a known frequency, ω_A and phase ϕ_A

$$[E^2_{sig} + E^2_{ref} + 2E_{sig}E_{ref}\cos(\Delta\omega t + \Delta\phi)][E_A\cos(\omega_A t + \phi_A)]\,, \tag{4.5}$$

which can be expanded and simplified to result in:

$$\begin{aligned} &(E^2_{sig} + E^2_{ref})E_A\cos(\omega_A t + \phi_A) + \\ &\qquad E_{sig}E_{ref}E_A[\cos((\omega_A - \Delta\omega)t + \phi_A - \Delta\phi) \\ &\qquad\qquad + \cos((\omega_A + \Delta\omega)t + \phi_A + \Delta\phi)]. \end{aligned} \tag{4.6}$$

In most instances passing this signal through a low pass filter would result in a zero signal as a result of the removal of all periodic terms. However in the case that $\Delta\omega = \omega_A$, the difference term becomes a constant signal and unaffected by the low pass filter, which we will define as:

$$X = E_{sig}E_{ref}E_A\cos(\phi_A - \Delta\phi). \tag{4.7}$$

This signal is now independent from the $E_{sig}^2 + E_{ref}^2$ component and their associated noise contribution. To compensate for environmental influence such as air flow and temperature change on the system the arbitrary frequency can be measured continuously to enable these shifts to be taken into account. This allows not only the relative intensity of the signal to be collected but can also enable the collection of the phase information. This is achieved by adding a $\frac{\pi}{2}$ phase shift to the arbitrary signal,

$$E_A\cos\left(\omega_A t + \phi_A + \frac{\pi}{2}\right) = E_A\sin(\omega_A t + \phi_A), \tag{4.8}$$

which when multiplied and treated with the same low pass filter the resulting signal, Y, is equal to:

$$Y = E_{sig}E_{ref}E_A\sin(\phi_A - \Delta\phi). \tag{4.9}$$

This is referred to as the quadrature component (Y), with the afore mentioned X in Equation 4.7 known as the in-phase component. Using these two signals it is possible to extract the amplitude, R, independent of the phase, as well as the phase, θ

$$R = \sqrt{X^2 + Y^2} \quad \text{and} \quad \theta = \tan^{-1}\left(\frac{Y}{X}\right). \tag{4.10}$$

Ultimately this results in a coherent detection system, able to perform shot noise limited detection of the reflected signal [79].

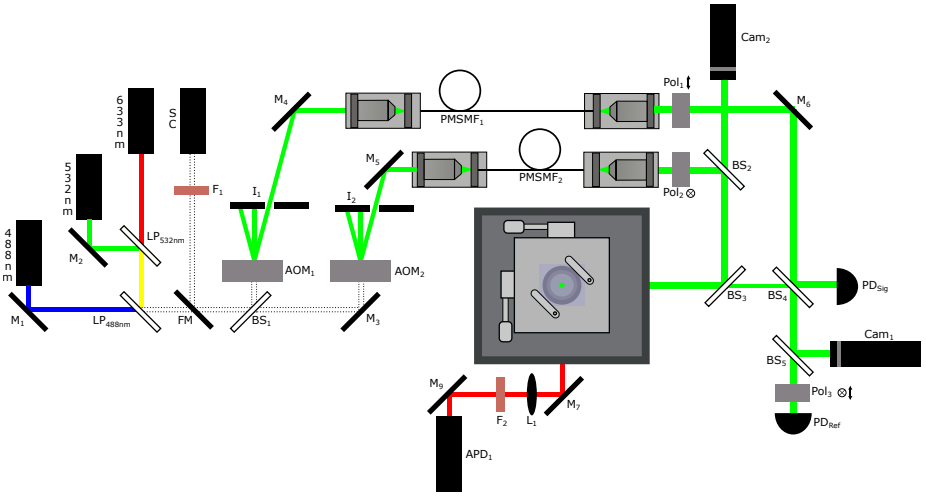

Figure 4.1: Schematic of ICPM where: SC is a supercontinuum source, F_i are notch filters, M_i are broad-band mirrors, FM is a flip mirror, BS_i are beam-splitters, $LP_{i\ nm}$ are long pass filters, AOM_i are acousto-optic modulators, I_i are irises, $PMSMF_i$ are polarisation maintaining single mode fibres, Pol_i are plate polarisers, L_i is a lens and APD_i are avalanche photo-diodes. For simplicity only the 532 nm laser line is depicted after the AOMs while the red output from the microscope body represents the fluorescence signal.

4.3 Build details

Here, following the beam path through the system as schematically depicted in Figure 4.1, the function of each section is explained starting with the laser sources. Four different laser sources are coupled into the system, a 633 nm HeNe (JDSU 1137P), a 532 nm diode pumped solid state (Oxxius LCX-532L), a 488 nm diode (Votran Stradus) and a super continuum source (Fianium SC-400PP), the latter is primarily used for fluorescence excitation. All the monochromatic sources are passed through the same beam splitter (BS_1) to generate a reference and a signal branch to form an interferometer. A combination of long pass filters ($LP_{1\text{-}2}$) and individual alignment mirrors($M_{1\text{-}2}$) enables complete overlap of all three wavelengths facilitating quick switching between each excitation wavelength. A notch filter, F_1, is used to select a wavelength from the supercontinuum source which is coupled into the system through a flip mirror, FM. Both the reference and signal arm are passed through separate Isomet 1205C-2

Acoustic Optical Modulator, AOM_1 and AOM_2, respectively, to enable heterodyne detection of the scattered signal.

4.3.1 Acoustic Optical Modulator

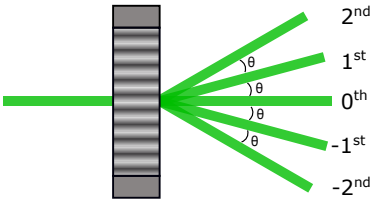

Figure 4.2: Depiction of the diffraction angle, θ, caused by the index grating in an AOM, with each order labelled.

AOMs are devices that act as tunable diffraction gratings. Through the acousto-optic effect an index grating is generated inside a crystal. By tuning the frequency of the applied acoustic wave the device can diffract the optical beam to a desired angle, as schematically depicted in Figure 4.2 and shown by:

$$\Lambda sin(\theta) = m\lambda\,, \tag{4.11}$$

where, Λ is the acoustic wavelength, θ the diffraction angle, m the diffraction order and λ the optical wavelength. Unlike a conventional diffraction grating the different orders experience a frequency shift which is related to the acoustic driving frequency of the crystal.

$$\nu_m \rightarrow \nu_o + mF\,, \tag{4.12}$$

where ν_o is the optical frequency and F the acoustic frequency. The shift in frequency can be utilised to enable heterodyne detection as discussed further in Section 4.2.4. This frequency shift however is in the radio frequency range and is difficult to detect optically without specialised electronics. For that reason a pair of AOMs is used to generate a lower frequency difference between the two branches. By selecting a small difference between the driving frequencies

of each AOM and selecting the 1st order from both AOM outputs. The interference between the two will result in the assigned difference frequency as the beating frequency. A frequency of 70 kHz is typically selected for historical reasons to allow detection without the requirement for expensive electronics. The diffraction angle of the modes are dependent not only on the driving frequency but also on the wavelength of the incoming beam, shown by Equation 4.11. It is therefore necessary to change the driving frequency when a different laser source is required so as to maintain a common path. This principle enables rapid switching between wavelengths if desired.

4.3.2 Fibres

Following the AOM both beams are focused into separate single mode polarisation maintaining fibres ($PMSMF_{1\text{-}2}$) to ensure that all wavelengths follow the same beam path. The in-coupling polarisation is aligned parallel with the transmission axis of the fibre ensuring maximum power transfer. Passing the beams through single mode fibres cleans the beams of aberrations generated by the AOMs and returns them to a well defined Gaussian. Both beams are outcoupled and collimated to 12 mm using a Nikon TU Plan Fluor 5x objective, this ensures that the imaging objective will be sufficiently overfilled and that the reference beam is of greater diameter than the resulting signal beam at overlap. Objectives are utilised here so that all wavelengths are focused onto the same focal plane. The outcoupling of the polarisation maintaining fibre is chosen so that the beam is polarised 45^{o} to the S and P axis to ensure that it is possible to switch the incident polarisation state through use of only the polarisers.

4.3.3 Microscope Body

The reference and signal branch are passed through orthogonally orientated thin plate Meadowlark Optics DPM-100-Vis polarisers ($Pol_{1\text{-}2}$) crossing the reference and signal beams. Thin plate polarisers are selected due to their higher thermal stability and reduced beam displacement upon rotation compared to

Glan-Thompson polarisers. The signal path is then aligned into the microscope body with a 2" beam splitter 90:10 (BS_2) and a 2" 30:70 beam splitter (BS_3) that enables a bright field camera (Cam_2) to image the sample surface. To the base of the microscope body a dichroic holder (Thorlabs CM1-DCH) is attached, shown in more detail in Figure 4.3. This enables the mounting of dichroics that are selected based on the fluorescent sample being investigated to ensure that excitation wavelengths are reflected and those collected for fluorescence measurements are transmitted to the Avalanche Photodiode (APD_1) below. A varying intensity across the beam width is present due to the Gaussian profile. To prevent this uneven intensity distribution from limiting the size of the focal spot the objective is overfilled by a factor of two reducing the intensity variation in the beam and therefore enabling the minimal focal spot size. This does however result in a reduction in available power to be used for illumination.

4.3.4 Scattering Signal

The signal, reflected from the sample, passes through the initial alignment beam splitter (BS_3) and is overlapped with the reference branch on a further beam splitter (BS_4). The orthogonally polarised overlapped beams are then split between two detectors, a reference detector (PD_{ref}) and signal detector (PD_{sig}). The combination of beams is directly focused onto the signal detector. For the reference detector they are first passed through a 45^o polariser. This is to ensure that both reference and signal beams can interfere and generate a beating frequency that can be used as a reference in heterodyne detection. The combined beams are also incident onto a Charged Coupled-Device (CCD) camera (Cam_1) to aid with overlapping and focusing of the beams. The signal detector will only be able to detect signal when a scattering particle is present in the focus, because of the scattered light containing some component of light parallel to the reference beams polarisation. This approach results in a collected signal that is free of the excitation beam yet still contains the required frequency information for heterodyne detection.

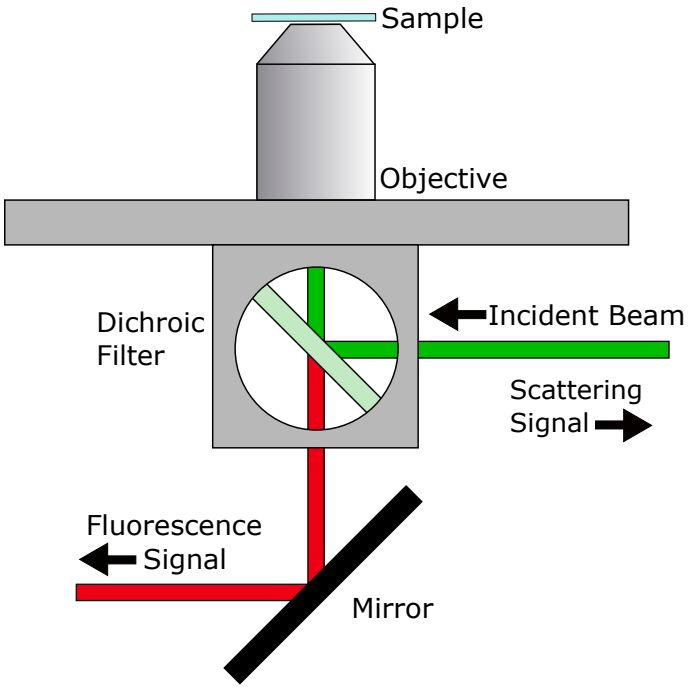

Figure 4.3: Diagram depicting the use of a dichroic filter to extract fluorescence signals from the scattering signal.

4.3.5 Fluorescence Signal

The fluorescence signal passed through the dichroic is focused by a 500 mm lens to ensure that only the central peak of the Airy ring pattern is detected by the APD (Perkin Elmer). The dichroic mounting cube, shown in Figure 4.3, is used to allow swapping out of different filters without a full realignment of the system. A secondary filter, F_2, specific to the investigated probe is utilised to further isolate the desired fluorescent signal detected by the APD.

4.4 Operating in reflection mode

To test the system a 68.2 μm $\times$ 47.5 μm array of nanorod pairs was fabricated and imaged in this reflection configuration. The results of the single image scan can be seen in Figure 4.4. This large scan was taken over $\sim$ 1 hour, with the fast axis along the x-axis and slow along the y-axis. The orientation and spacing

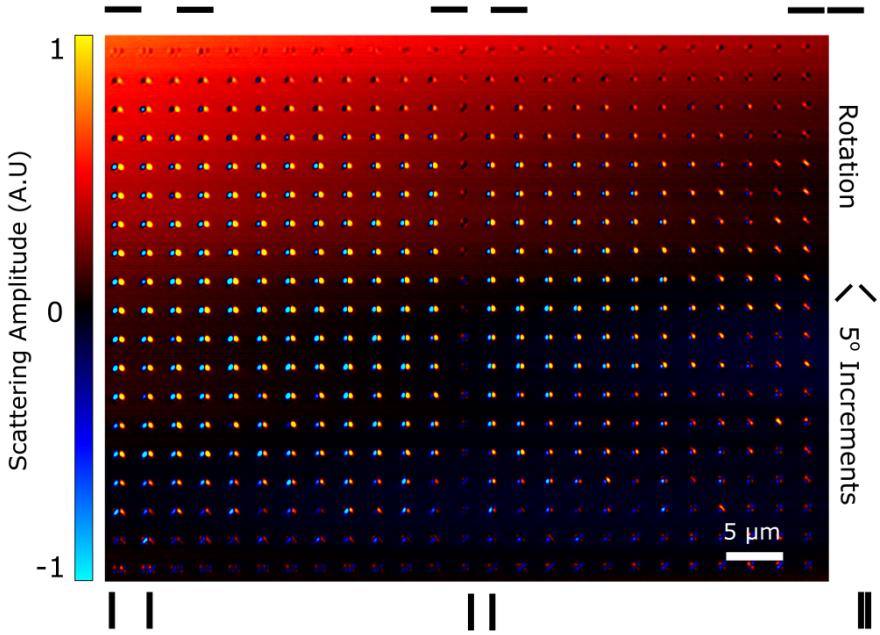

Figure 4.4: 68.2 μm $\times$ 47.5 μm scattering image of nanorod pair array collected in reflection with a 0.9 NA objective. The 40 nm $\times$ 240 nm nanorods are rotated by 5° increments along the y-axis and their separation decreased in 25 nm increments along the x-axis, as depicted around the image.

of the nanostructures are schematically shown along the outside of the image. There is a clear detection of each nanostructure with a good signal to noise ratio of $\sim$ 30 for these nanostructures. Individual 40 nm $\times$ 240 nm rods, with a height of $\sim$ 20 nm, are also present and detectable on this sample, though do produce a much smaller signal to noise ratio of $\sim$ 6. A slow shift in scattering amplitude from the background can be seen along the slow axis, $\sim$ 2% across the image. This shows that some drift still occurs however not significant enough to prevent the detection of the nanostructures. The gradual drift across the image appears to not align directly to the slow axis of the image as would be expected for system drift over time. This suggests that in actuality the sample mounting onto the stage was not flat and therefore would contribute significantly to this varying background signal. With the assumption that the silicon substrate is sufficiently flat an active focus control could be implemented to overcome this variation, adapting the focus depending on the background value. The func-

tionality of the system is not severely hindered by this factor as shown in the following chapters where similar nanofabricated samples are analysed using the presented system.

Throughout this chapter the design and function of interferometric cross polarised microscopy implemented in reflection has been discussed. Using a 0.9 NA objective the system was capable of imaging a large 68.2 μm $\times$ 47.5 μm array of nanostructures with a signal well above any drift presented.

Chapter 5

Orientation Detection of Nanorods with Interferometric Cross Polarised Microscopy.

As a means of imaging biological systems asymmetric scattering particles have an advantage over commonly used spherical particles; they can additionally capture rotational information. This chapter presents interferometric cross polarised microscopy as a means of determining the orientation of such asymmetric particles through monitoring of the spatial distribution of the scattering signature. A theoretical model to explain the changes in distribution is also presented.

Fluorescent molecules are often used to probe biological systems but understanding complex biological systems such as ATPase [80], enzymes [81] and molecular motors [82] requires not only location information but also rotational information. Fluorescent molecules through their dipole nature have been employed to collect this information [83–85], however it is well known that such molecules suffer from bleaching [86], making long term studies difficult and as a result of the fluorescence lifetime have limited time resolution. This can be overcome through the application of asymmetric gold nanoparticles in biological imaging. These particles do not suffer from bleaching when used as markers [87], enable higher time resolution [32] and are non-toxic under the right conditions [88,89].

The response of asymmetric nanoparticles to polarised light depends on their relative angle [87], allowing the detection of their orientation in a similar way as used for fluorescent molecules [90]. To apply asymmetric gold nanoparticles in biological imaging a number of hurdles need to be overcome; the main one is ensuring sufficient contrast between the particle and the scattering medium of the cell while maintaining the ability for nanoparticles to enter into and move inside a biological sample. Cell uptake and internal transport of nanoparticles is dependent on the size of the nanoparticles [91]; therefore using the smallest possible size increases the regions of the cell that can be probed as well as minimising the potential influence of the particle on the biological process of interest. The drawback is that the scattering signal is proportional to the square of the volume, drastically reducing the detected signal. A diverse number of optical techniques have been developed to detect nanoparticle asymmetry inside cells including: defocused dark field microscopy [25, 92], the use of high order laser modes [93, 94] and the application of photothermal microscopy [95]. These techniques have also been utilised for determining the full 3D orientation of individual nanorods [25, 92, 95].

In this chapter an investigation into the ability to determine the full 3-D orien-

tation of individual nanorods through the analysis of the spatial distribution of the scattering signature is presented. Interestingly it is found that the nanorods aspect ratio is of high importance to their use to resolve their full 3-D orientation.

Interferometric Cross Polarised Microscopy (ICPM) is a confocal-like imaging approach able to detect individual nanoparticles down to 5 nm in diameter [96]. The experimental layout for ICPM used in the work is shown in Figure 5.1(a) and explained in detail throughout Chapter 4. Two branches of orthogonal polarisation states are created, that form a reference and a signal branch. Focusing the signal branch using a high NA objective projects the incident linear E_x polarised light onto all three planes [62], the spatial fields of each of the field components is shown in Figure 5.1(b) - (d) for E_x, E_y and E_z, respectively. For clarity, the E_y and E_z components are scaled by the value in the bottom left of the image so that they are of approximately equal magnitude to the E_x component. By interfering the signal from the sample with the orthogonally polarised reference beam only the signal from the E_y component can contribute, resulting in almost background free detection. Here acoustic-optic modulators (AOM) shift the beam frequencies in the two branches resulting in a small frequency difference between the signal and reference enabling heterodyne detection of the interference signal generated from the two beams to remove the remaining background [79].

Due to the asymmetry of the nanorods and the polarisation dependence of ICPM, an orientation dependent response is expected. As a first step towards investigating this in detail the 2-D situation is examined to simplify explaining the observed system response. For this purpose a series of nanorod structures were fabricated using a combination of e-beam lithography and thermal evaporation. The sample was prepared on a type 1.5H Marienfeld cover glass through the evaporation of a 2.5 nm chrome adhesion layer followed by a 23 nm layer of gold to form the nanorod arrays. A series of rods were fabricated in this

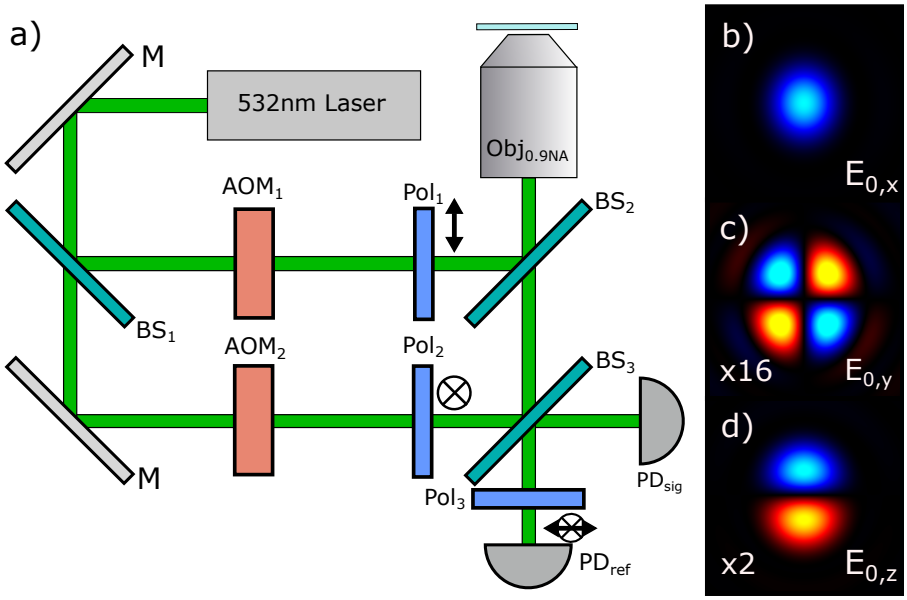

Figure 5.1: (a) Experimental layout for ICPM, BS are beam splitters, M are mirrors, AOM_i are acoustic-optic modulators, Pol_i are polarisers, Obj is an 0.9NA objective and PD are photodiodes. (b) - (d) show the E_x, E_y and E_z field components respectively, as a result of the strong focusing of linearly x-polarised light. (c) and (d) are scaled to an equal magnitude as that seen in (b) and are 1.3 μm $\times$ 1.3 μm.

way varying both the aspect ratio and their orientation. This rotation of the nanorods throughout a single sample simulates a rotated polarisation in a single image without the need to adjust optical components of the setup. Characterisation of the sample, to enable a direct comparison between the fabricated structures and optical signal, was conducted through high-speed atomic force microscopy [97], to determine the quality of the fabricated asymmetric structures with a varying angle. This data revealed inconsistencies with the height and shape of the structures, a result from cleaning the sample with a high power O_2 plasma clean. The etching from this cleaning step results in both reduction of the height from the expected 23 nm to $\sim$10 nm and a greater variation of the structures' height across the sample.

The incident beam was at 532 nm to be close to the plasmonic resonance of the transverse mode of the rod structures, which remains constant across the

varying rod aspect ratios. Imaging of a point particle with ICPM results in a scattering signature that closely resembles the E_y component shown in Figure 5.1(c) which was discussed in detail previously [63]. To investigate the effects an asymmetric scatterer has on the scattering signal, Figure 5.2 presents the scattering signatures for nanorods with high aspect ratios (5, 7 and 9) under five different orientations of the nanorod with respect to the incident polarisation. AFM images for these same nanorods is presented in Figure 5.2. Here a high aspect ratio was selected to ensure that any effect is clearly visible in the scattering signal. At an angle of 0^o the rods major axis is parallel to the incident polarisation, seen in Figure 5.2 across all three example aspect ratios. As expected the structure is very similar to that seen from a point scatter, a pure E_y component, as simulated in Figure 5.1(c). However elongation of the scattering signature along the major axis of the rod is clearly visible in the nanorod with the highest aspect ratio. In this case the rods major axis has a length of $\sim$380 nm, greater than the diffraction limit for a wavelength of 532 nm, resulting in a noticeable elongated structure, similar to that which would be seen with a series of closely spaced single scatterers. A rod rotated by 20^o with respect to the incident polarisation, seen in Figure 5.2, produces a stark change in scattering signature. There is a distinctive shift from the cloverleaf distribution, seen at 0^o, to a elongated Gaussian along the diagonal. As seen from the presented angles between these extreme values there is no sudden switch in structure visible. The degree with which the distribution changes is however clearly dependent on the angle of the rod relative to the incident polarisation.

To explain this behaviour an analytical model for electrostatic polarisability, as used by Al-Qadi and Saiki [98], is presented. In order to be able to provide physical insights the nanorods are modelled as prolate spheres with their major and minor semiaxis denoted with a and b, respectively, as shown in Figure 5.3(a), rather than the more accurate representation of capped rods, the shape seen with AFM. Such an assumption will have an effect on the calculated optical

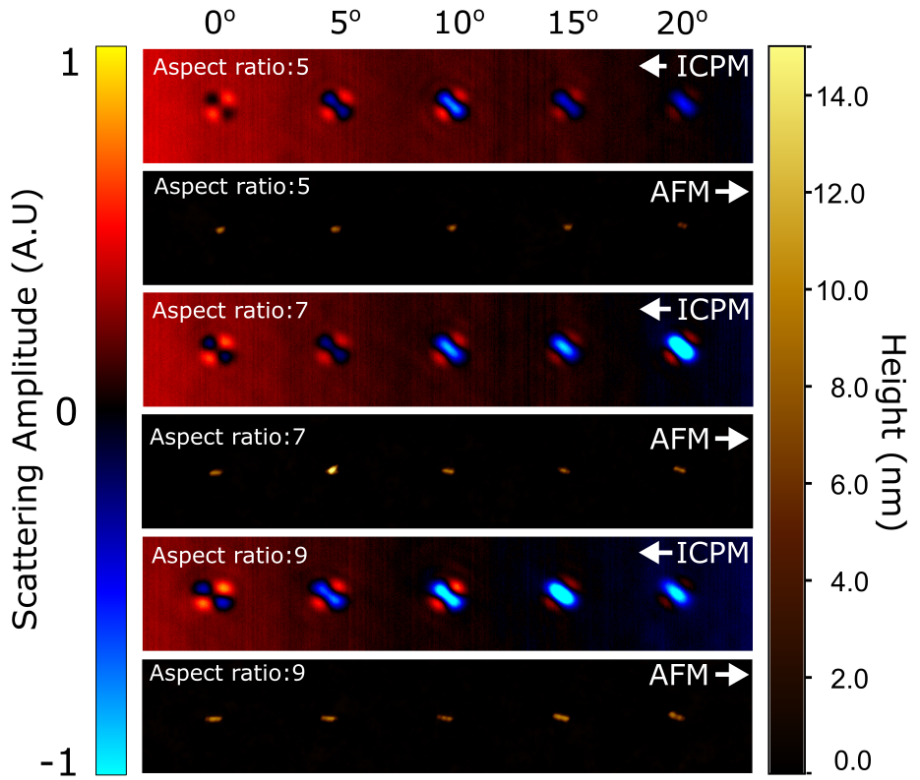

Figure 5.2: The scattering signatures produced when a rotating asymmetric particle is imaged through ICPM. Three different aspect ratios (length/width), with a fixed width of 40 nm, nanorods are presented with varying angles relative to the incident polarisation. All 13 μm x 2.7 μm images are taken from the same sample and scan. AFM data for the rod structures are presented below each ICPM image. Width of all rods is 40 nm, varying in length according to their aspect ratio. AFM images collected by Loren Picco [97].

properties, such as the plasmon wavelength, as shown by Myroshnychenko *et al.* [99]. Due to a lack of an analytical solution for the capped rod case however the prolate sphere approach is used. The electrostatic polarisability of a prolate sphere is given by:

$$\alpha_i = \frac{ab^2}{3} \frac{\epsilon_p(\omega) - \epsilon_m}{(\epsilon_p(\omega) - \epsilon_m)L_i + \epsilon_m}, \tag{5.1}$$

where ϵ_m and ϵ_p denote the medium and rod dielectric constant respectively and L_i is a geometrical factor [100] as given in Equations 5.2 - 5.4 for the case of a prolate sphere, with $a > b$:

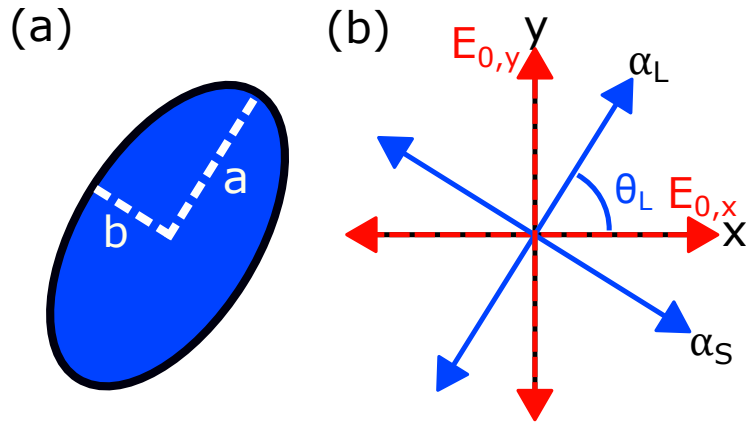

Figure 5.3: (a) Diagram of a prolate sphere annotated with the notation used to describe the shape of a rod.(b) Notation used throughout the discussion, where α_L lies along the rods major axis and α_S the minor axis. x and y give the lab frame of reference.

$$L_a = \frac{1-e^2}{2e^3}\left(log\left(\frac{1+e}{1-e}\right) - 2e\right) \tag{5.2}$$

$$L_b = L_c = \frac{1}{2}(1 - L_a)\,, \tag{5.3}$$

where

$$e = \sqrt{1 - \frac{b^2}{a^2}}. \tag{5.4}$$

The dipole moment induced by the excitation light is given by $P_i = \alpha_i E_0$. Due to the varying angle of the rod axis in relation to the incident polarisation it is required that the projection of $E_{0,x}$ is calculated for each axis. A diagram of the used notation is provided in Figure 5.3(b). This diagram illustrates that a linearly polarised beam along the x-axis, $E_{0,x}$, will project a component $E_{0,x}cos(\theta_L)$ onto the α_L axis and $E_{0,x}sin(\theta_L)$ onto the α_S axis. Each of these α_L and α_S components has a component along the x and y axis; these projections can be expressed in the following equations for the scattered field along the two lab frame axis, x and y:

$$E_{scat,x} = \alpha_L E_{0,x}\, cos^2(\theta_L) + \alpha_S E_{0,x}\, sin^2(\theta_L) \tag{5.5}$$

$$E_{scat,y} = E_{0,x}(\alpha_L\, cos(\theta_L)\, sin(\theta_L) - \alpha_S\, sin(\theta_L)\, cos(\theta_L)) \tag{5.6}$$

$$= \frac{E_{0,x}}{2}\, sin(2\,\theta_L)\,(\alpha_L - \alpha_S) \tag{5.7}$$

As discussed above the high NA objective used in ICPM generates a field component along the y-axis, $E_{0,y}$, which will also contribute to the induced dipole moment, in a similar way as is the case for $E_{0,x}$. This leads to the following final expressions for the scattered fields in x and y directions, respectively,

$$E_{scat,x} = E_{0,x}[\alpha_L\, cos^2(\theta_L) + \alpha_S\, sin^2(\theta_L)] + \frac{E_{0,y}}{2}\, sin(2\,\theta_L)\,(\alpha_L - \alpha_S) \tag{5.8}$$

$$E_{scat,y} = \frac{E_{0,x}}{2}\, sin(2\,\theta_L)\,(\alpha_L - \alpha_S) + E_{0,y}[\alpha_S\, cos^2(\theta_L) + \alpha_L\, sin^2(\theta_L)] \tag{5.9}$$

While this model accounts for the dielectric constants and particle shape it is only valid for particles much smaller than the incident wavelength. The particles imaged here lie outside these parameters and therefore a correction to these equations is required [98]. For this the modified long-wavelength approximation is used to account for both radiative damping and the depolarisation effects arising due to the greater size. This corrected polarisability for both the major and minor axis is given by:

$$\alpha_L^* = \frac{\alpha_i}{1 - \frac{2}{3}ik^3\alpha_i - \frac{k^2}{2a}\alpha_i}\,, \tag{5.10}$$

$$\alpha_S^* = \frac{\alpha_i}{1 - \frac{2}{3}ik^3\alpha_i - \frac{k^2}{2b}\alpha_i}\,, \tag{5.11}$$

where α_L^* and α_S^* denote the major and minor polarisability respectively, with the wavenumber given by k. As a result of the crossed polarised nature of ICPM only the $\mathrm{E_{scat,\,y}}$ component can interfere with the reference and the detected signal is therefore:

$$E_{sig} = \Big(\frac{E_{0,x}}{2}\, sin(2\,\theta_L)\,(\alpha_L^* - \alpha_S^*) + E_{0,y}[\alpha_S^*\, cos^2(\theta_L) + \alpha_L^*\, sin^2(\theta_L)]\Big) E_{ref}\, cos(\phi_a)\,, \tag{5.12}$$

where E_{ref} is the reference E-field and ϕ_a is the phase difference between the signal and reference beams. From Equation 5.12 it can be seen that the resulting signal will always have a component dependent on $E_{0,y}$ and therefore will be dependent on the spatial distribution of the excitation seen in Figure 5.1(c). For the $E_{0,x}$ component, for which a spatial distribution shown in Figure 5.1(a) is expected, this is not the case. For symmetric ($\alpha_L^* = \alpha_S^*$) or when $\theta_L = 0^o$, 90^o, the contribution from the $E_{0,x}$ component is zero as expected. This can be seen in the optical data in Figure 5.2: for a rotation of 0^o there is no $E_{0,x}$ field contribution, visible as the spatial distribution closely resembling the $E_{0,y}$ contribution seen in Figure 5.1(c). Increasing the angle results in a contribution from $E_{0,x}$, increasing in strength the greater the angle, as seen by the deviation from the initial spatial distribution.

Figure 5.4 compares the predictions of Equation 5.12 for a rod with ratio 7 with that of the collected experimental data for a rod of ratio 7 through a rotation of 0^o - 20^o. The simulated data is scaled uniformly across the angles to match the colour scale of the experimental data. There is a clear correlation between the predictions of Equation 5.12 and the experimental data showing a very similar qualitative transition from the pure $\mathrm{E_{0,y}}$ spatial distribution at zero degrees. While there is good agreement in the distribution it is not fully

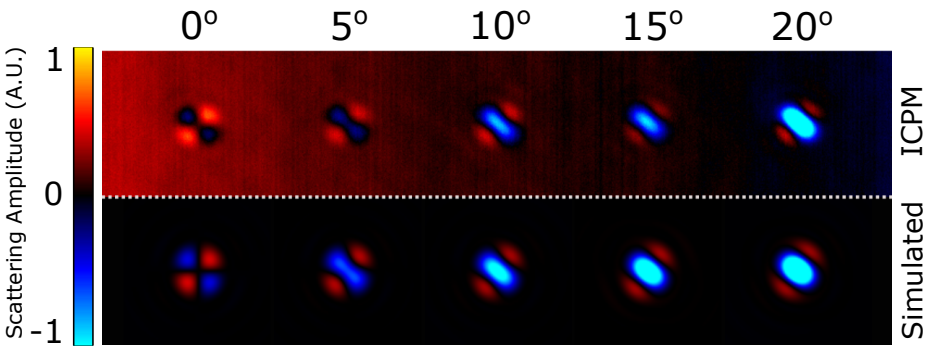

Figure 5.4: Comparison between the collected signal (top) at various angles with a rod ratio of 7 and the simulated signal (bottom) produced from Equation 5.12 using a rod ratio of 7. Each image is 4.2 μm x 2.5 μm. Background value for the experimental data is shifted throughout the single image as a result of sample levelling, this is not accounted for in the simulated signal, leading to a deviation between the colour schemes.

shared in terms of magnitude, as is most notable at 15°. These discrepancies make fitting the data to the theory difficult without adjustments to the intensity profile. The cause of this disagreement is attributed to poor fabrication quality, as highlighted in the AFM image in Figure 5.2 that shows deviation from the expected structure. Inconsistent heights and shape will greatly change the volume of the structure; directly affecting the amount of scattered signal. Figure 5.4's experimental data also depicts a shift in background intensity throughout the sample which is the result of experimental phase drift, suspected to come from the sample not being level on the sample stage. This shift results in an apparent discrepancy between the first two angles as a result of the phase shift not being accounted for in the simulation and therefore resulting in a skewed colour scheme. The angular range is kept between 0° - 20° for this figure due to the comparative magnitude of $E_{0,x}$ to $E_{0,y}$ and therefore the speed with which the $E_{0,x}$ component increases and begins to dominate the observed spatial structure. The result from this rapid saturation is a reduction in sensitivity at lower angles using only spatial information. Equation 5.12 reveals that this can be overcome through the use of a significantly lower rod ratio, this is highlighted in Figure 5.5(a). Figure 5.5(a) presents the simulated contribution from the $E_{0,x}$

mode, where ϵ_p is taken as $-5.71 + 2.16i$ for gold [98] and ϵ_m as $1.0 + 0i$ for air. The reduced contribution of the $E_{0,x}$ distribution at lower ratios makes it more sensitive for higher angle determination, where the contribution from $E_{0,x}$ would begin to saturate the signal for higher ratio rods. Figure 5.5(b) shows the simulated relative contribution for a number of different rod ratios. The variation in magnitude for different ratios could be utilised as a method of determining the ratio of a given structure from its scattering distribution.

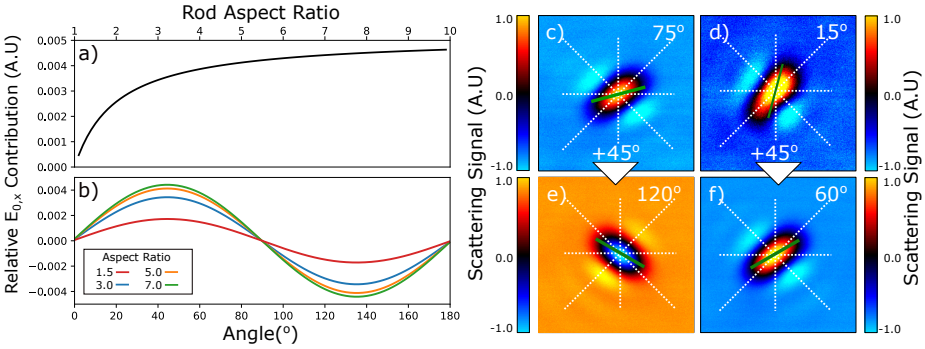

Figure 5.5: (a) and (b) presents the relative $E_{0,\,x}$ contribution for different rod ratios and angles, respectively, as predicted by Equation 5.12. (a) Is calculated for a rod angle of 45° with (b) depicting ratios of 1.5, 3, 5 and 7 in red, blue, orange and green, respectively. (c) and (d) show two gold nanorods rotated 75° and 15°, respectively, to the incident polarisation. (e) and (f) show the effect when the orientation of the sample is rotated 45°. The green lines in (c), (d), (e) and (f) represent the major axis direction of the rods, not to scale, with each image sized at 1.9 μm x 1.9 μm.

Equation 5.12 describes a $\sin(2\theta_L)$ dependence for the $E_{0,x}$ contribution. This periodic dependence results in an identical response for multiple angles throughout a 180° rotation of the rod, significantly hindering the full identification of the orientation. An example of this behaviour is shown in Figure 5.5 (c) and (d) where the response of a rod rotated at 15° and 75° to the incident polarisation, respectively, is presented. The spatial distribution from these two signals are very similar, resulting in difficulty in identifying their orientation. Theoretically the distribution seen in Figure 5.5(c) and (d) would be identical however inconsistent fabrication between the structures results in some varia-

tion. To overcome the inability to differentiate between the two angles, the $E_{0,x}$ spatial distribution, seen in Figure 5.1(c), can be utilised. The $E_{0,y}$ component is made up of four lobes, where adjacent lobes have opposite phase, as seen by the different colours in Figure 5.1(c). For asymmetric particles this phase structure influences the phase of the scattered signal. The orientation of the rod will determine which lobe of the $E_{0,y}$ structure is probed. Figure 5.5(c) shows a rod orientated at 75° to the incident polarisation, the green line shows how this orientation probes the top right and bottom left lobe. Figure 5.5(e) depicts a rod at 120° to the incident polarisation resulting in the top left and bottom right lobes being probed, resulting in an opposite phase to that seen in Figure 5.5(c). Not only is there a change in phase but a clear change in spatial distribution is also seen, arising from the interaction of the phase with the $E_{0,x}$ component. This phase information therefore enables the determination of which quadrant the rod is positioned. This overcomes a $\sin(\theta_L)$ dependence but not the $\sin(2\theta_L)$ seen in Equation 5.12. To address the 2θ dependence this phase shift can be utilised through two measurements. Consider the issue with determining the angles for Figure 5.5(c) and (d), and the phase shift resulting from changing lobes. If the sample in Figure 5.5(c) is rotated 45° relative to the incident polarisation a phase shift is detected, seen in Figure 5.5(e). The structure has been rotated into the opposite phased lobe. If the same 45° is conducted on Figure 5.5(d) no change in phase is identified, the rotation is not large enough to probe the opposite phased lobe, maintaining the same phase, seen in Figure 5.5(f). By rotating the sample or the excitation and detection polarisation between two measurements and monitoring the phase shift, in combination with determining the $E_{0,x}$ and $E_{0,y}$ component contributions the full 2D orientation can be determined.

Here a method to use ICPM to identify the 2D orientation of a single nanorod structures has been discussed. Given the presence of all 3D field components in the focus, ICPM has the potential to retrieve the full 3D orientation using

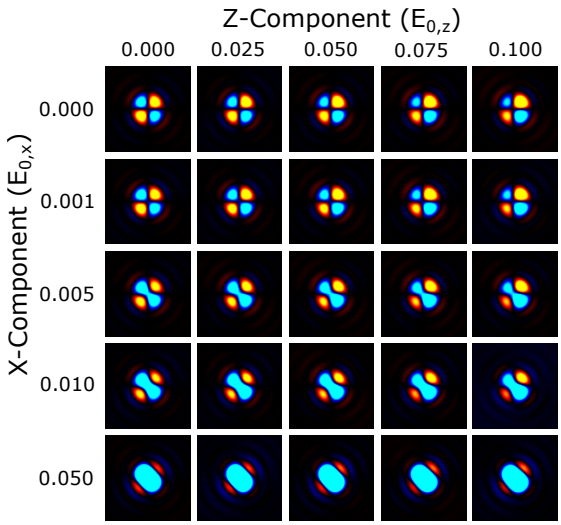

Figure 5.6: Simulated scattering distribution for a varying combination of $E_{0,x}$ and $E_{0,z}$ components. Consistent scaling is used across all images resulting in clipping at high x-components. Each image is 1.9 μm $\times$ 1.9 μm.

the different spatial symmetries of the field components shown in Figure 5.1(b) - (d). Examples of images resulting from combined $E_{0,x}$, $E_{0,y}$ and $E_{0,z}$ components can be seen in Figure 5.6. Interestingly the addition of a z-component introduces an asymmetry between lobes that is not visible for combining only E_x and E_y. This asymmetry is routinely observed in our experiments indicating that E_z plays an important role in the scattering distribution, as highlighted in Chapter 3. The collected experimental data could be processed in a similar way as the 2D situation, determining the contribution from each of the three spatial structures and using their relative values to deduce the orientation in 3D space.

Throughout this chapter the effects of asymmetric particles imaged using ICPM have been investigated. It has been shown, that the projection of the various field components, resulting from focusing by a high NA objective, have a distinct effect on the scattering signature produced by an asymmetric particle. This resulting dependence of the observed scattering signature on the particles orientation does potentially enable the identification of a particles orientation, which is shown in 2D through a combination of theory and imaging of nanofab-

ricated samples. While not achieved here, there is indication that the ratio can also be retrieved enabling greater characterisation of the nanorod. This however depends on the ability to decouple the angular and aspect ratio terms in Equation 5.12. This approach could be further extended to resolve the full 3D orientation of nanorods using the distinct spatial distribution of the different fields in the focus of an high NA objective.

Chapter 6

Nanogap detection with Polarised Optical Microscopy.

Nanometre sized gaps are common within nanoscience but are difficult to measure in real time during their fabrication. Optical imaging is ideally suited to the task but the diffraction limit prevents imaging at the required length scales. Throughout this chapter interferometric cross polarised microscopy is utilised as a means of detecting the separation of two nanodisks, where a gap size of 20 nm is found to be easily detectable.

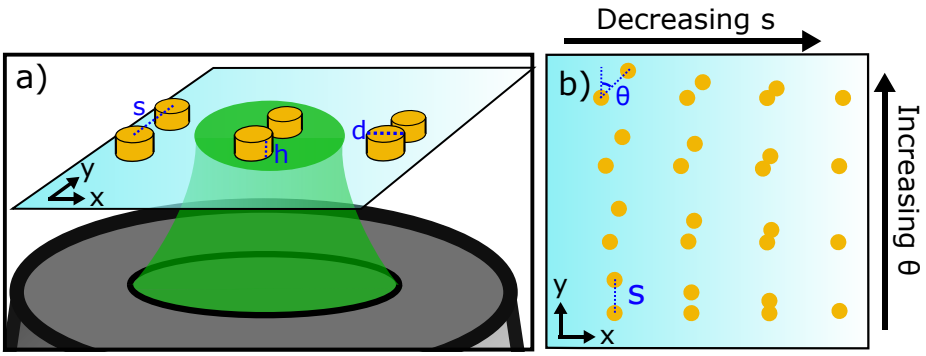

Figure 6.1: (a) Conceptual diagram of the optical detection of a gap between two gold disks. Where s is the separation between disks, d the disks diameter and h their height. (b) A simplified layout of the array of disks used, where θ represents the angle of rotation from the y-axis. The full array ranges from a separation of 0 nm to 600 nm in 25 nm increments and rotates from 0° to 90° in 5° increments.

The ability to fabricate gaps on the nanometre scale is utilised in a large number of applications including surface-enhanced Raman spectroscopy [101], biosensing [102, 103] and in fundamental electrical components [104] such as switches and rectifiers. Fabricating such small gap sizes is not an easy task but can be achieved through a range of techniques, including deep UV and electron beam lithography [105], as well as by the self assembly of nanoparticles [106]. The exact purpose of the gap determines the specific size requirement in each of these applications but is typically required to be significantly less than 50 nm, some requiring gaps as small as 1.3 nm [107]. Such small gap sizes limit the possible techniques for detecting and characterising their properties. Due to the diffraction limit, optical techniques generally have an insufficient resolution, leading to the requirement for alternative methods such as Scanning Electron Microscopy (SEM) and Atomic Force Microscopy (AFM).

These methods however have their own limitations, SEM is for example limited to conductive samples and has to be conducted in vacuum environments. Conventional AFM is a slow process for large arrays, especially if high resolution is desired and is dependent on the size of the tip, with some structures

requiring specialised high aspect ratio AFM probes. Moreover as AFM is a contact technique there is also the risk of causing damage to the sample. While some of these issues can be overcome using modifications, such as spin coating conductive layers or newer techniques such as High Speed AFM [97], an all-optical method would provide a simplified approach, providing both speed, ease of use and through its non-contact nature, would not have the potential to alter the sample. Optical methods could also be applied with relative ease during the fabrication process [108], resulting in greater control for processes such as etching. In this chapter an all-optical detection technique is used to detect gap sizes far below the diffraction limit through utilisation of the decomposed modes generated in the focus of a high NA objective. This approach has previously demonstrated detection down to individual 5 nm gold nanoparticles [96].

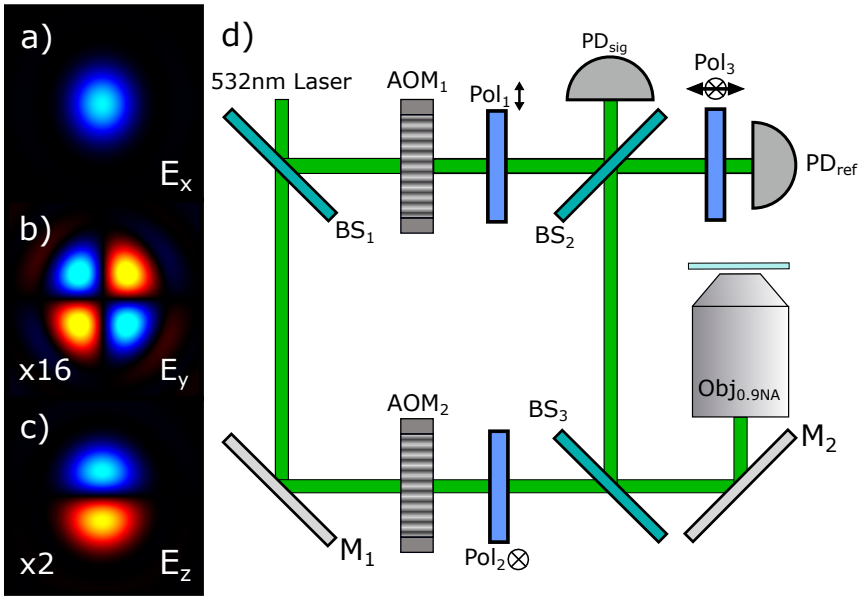

Figure 6.2: (a) - (c) show the simulated spatial modes for the E_x, E_y and E_z component of the field, respectively, that result from the strong focusing of linearly polarised light along the x-axis. For clarity the value in the bottom left of (b) and (c) depict the relative scaling. (d) The experimental layout where, BS_i are beam splitters, M_i are mirrors, AOM_i are acousto-optic modulators, Pol_i are polarisers, Obj is the objective and PD are photodiodes.

It is well established that the field in the focus of a high NA objective can be de-

composed into different spatial modes for X, Y and Z components of the field [62] denoted throughout as E_x, E_y and E_z, respectively. These field components are depicted in Figure 6.2(a), (b) and (c) for E_x, E_y and E_z, respectively.

As a result of the fact that each spatial mode exists in a different polarisation state, the use of an appropriately polarised local oscillator allows the isolation of a single spatial component. For this application the E_y spatial mode as depicted in Figure 6.2(b) is utilised, using the experimental setup, depicted in Figure 6.2(d), to selectively detect this spatial mode. This spatial mode is selected due to its asymmetric phase structure that should enable differentiation between closely spaced particles.

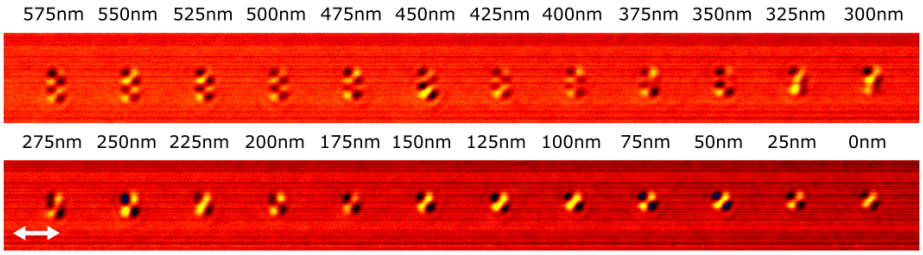

Figure 6.3: Scattering distribution for a pair of 80 nm diameter disks moving closer together, showing the separation along the y-axis. The incident polarisation is denoted by the white arrow. Separation distance is taken from the centre of each disk and labelled above each particle pair.

To investigate the detection limits resulting from imaging with the E_y spatial distribution, an array of disk structures, consisting of pairs of disks with a varying gap size, are fabricated with e-beam lithography and thermal evaporation. Each individual disk is ~25 nm in height with a diameter of 80 nm, with a centre to centre separation increasing in 25 nm steps from 0 nm to 600 nm, as conceptually depicted in Figure 6.1(b). Each pair is then rotated through 90° in 5° increments. Here both centre-to-centre separation and rotation are varied, to enable the investigation of the effect of the orientation of the structure on the polarisation detection. Figure 6.3 shows the scattering signatures produced

when particle pairs with a separation axis perpendicular to the incident polarisation are imaged. As expected for a diffraction limited optical system, the detected scattering signatures are first seen as two distinct signatures, as seen at a separation of 575 nm. As they move closer the resulting signature is an elongated version of the original point spread function, as seen at 250 nm. Below 200 nm the particles signature is individually indistinguishable from a point particle, as is the expected result for a diffraction limited approach. However for a rod pair that is orientated 45° to the incident polarisation this changes dramatically, as shown in Figure 6.4. The signatures merge in a similar fashion when a gap between particles is present, as seen from 575 nm to 100 nm. However when the disks touch there is a distinct difference in the detected scattering distribution as seen from the sharp transition between 100 nm and 75 nm.

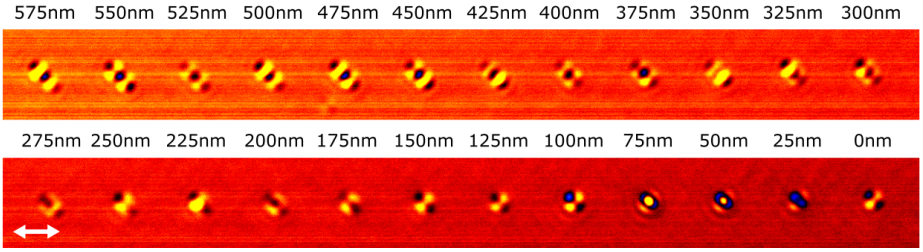

Figure 6.4: Scattering distribution for a pair of 80nm diameter disks moving closer together, a separation axis at 45° degrees clockwise to the incident polarisation. The incident polarisation is denoted by the white arrow. Separation distance is taken from the centre of each disk and labelled above each particle pair.

It is apparent from these results that there is a strong dependence on the angle of separation relative to the incident polarisation. The sharp change in spatial distribution arises upon contact between the two disks, this changes the nature of the particles. Rather than being circle symmetric as individual particles they become a single asymmetric object and behave more like a rod structure than a point particle. Investigating the transition from separated disk to a single isolated rod shape using these two polarisations therefore informs the cause for the change in scattering pattern. Given how the system isolates the $E_{0,y}$ spatial

mode through cross polarisation the system is intrinsically polarisation dependent. Asymmetric scattering structures have a notable effect on the polarisation state of the scattered light. Should a rod not be orientated parallel or perpendicular to the incident polarisation state, some of the scattered light will be projected onto the orthogonal axis. As shown in Chapter 5 the resulting spatial distribution of these projections can be described by:

$$E_{sig} = \frac{E_{0,x}}{2}\, sin(2\,\theta_L)\,(\alpha_L - \alpha_S) + E_{0,y}[\alpha_S\, cos^2(\theta_L) + \alpha_L\, sin^2(\theta_L)]\,, \qquad (6.1)$$

where $E_{0,x}$ and $E_{0,y}$ are the field distributions in the focal plane shown in Figure 6.2(a) and (b), respectively. θ_L is the angle between the long axis of the asymmetric structure and the incident polarisation with α_L and α_S as the polarisabilities of the long and short axis, respectively. Using Equation 6.1 it is possible to simulate the expected spatial distribution for different separations. A direct comparison between the simulated distribution and the signal collected is shown for the transition area in Figure 6.5. The close correlation between the simulated and collected data indicates the cause for the sudden change in spatial distribution. For circular symmetric particles such as the individual disks $\alpha_L = \alpha_S$. With this condition only the spatial distribution from $E_{0,y}$ is detected, as seen in Figure 6.5, up to 100 nm separation. Once there is contact between the two particles this condition is no longer true and the $E_{0,x}$ spatial distribution contributes to the detected signal resulting in a significantly different distribution. The elongated Gaussian detected can be explained through considerations of the phase structure of the $E_{0,y}$ spatial distribution. As highlighted in Figure 6.2(b) adjacent lobes have opposite phase, when combined with the $E_{0,x}$ Gaussian, shown in Figure 6.2(a). Two of the lobes enhance the signal while the other two will be reduced as a result of the respective phase relationship. The result is a elongated Gaussian at a $\sim$45^o angle.

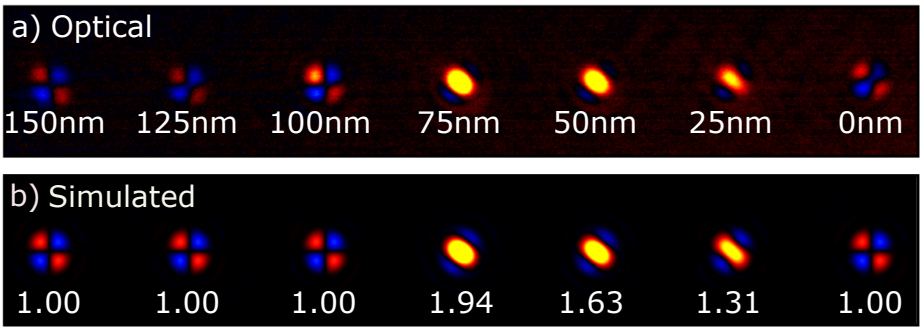

Figure 6.5: Scattering distribution for a pair of 80 nm diameter disks moving closer together and the simulated signal for different aspect ratios mimicking the separation, (a) and (b) respectively.

Given the known spatial distribution for both $E_{0,x}$ and $E_{0,y}$ component and that the resulting scattering signature is a combination of these two in different magnitudes, as shown by Equation 6.1, it is possible to fit each signal with a simulated distribution. This fit identifies the ratio of the $E_{0,x}$ and $E_{0,y}$ component contributions required to generate the detected distribution. This has the potential to provide a quantitative measurement for the gap size. Figure 6.6 plots this ratio, from the data with crosses and with the simulated ratio depicted with the solid line. As discussed previously, Equation 6.1 shows that two individual particles produce a scattering signature with no $E_{0,x}$ axis component. When the particle pair is no longer in contact, an 80 nm separation for this sample, the effective aspect ratio drops to one. This drastic aspect ratio change is seen in the experimental data; showing that a gap size of 20 nm, a value far lower than the diffraction limit, is easily detectable. The simulated results demonstrate how a spacing greater than 80 nm results in zero contribution from the $E_{0,x}$ component, this is however not apparent from the experimental data in Figure 6.6. The reason for this discrepancy is put down to imperfect fabrication of this specific sample. Any small asymmetries in the fabricated particle will result in a slight contribution of the x-axis modal component as was shown in Chapter 5. It should also be considered that any height variation

in the particle may result in the generation of an $E_{0,z}$ component, a factor not considered by the model or fitting parameters.

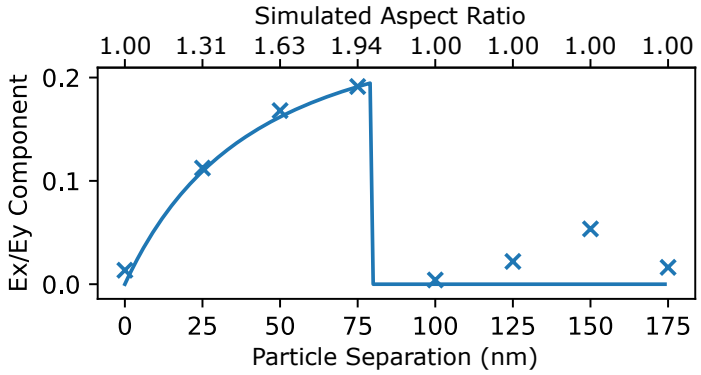

Figure 6.6: The relationship between the ratio of fitted signatures' $E_{0,x}$ and $E_{0,y}$ component contribution and the distance separating the two 80nm diameter nanodisks. The crosses show the collected experimental data with the solid line depicting the theoretical values.

The abrupt drop in ratio seen in the simulated data in Figure 6.6 would suggest that an infinitesimally small gap size could be detected. In reality this is due to the limitation of the model used. Equation 6.1 only accounts for asymmetries and the resulting polarisation effects, completely ignoring any inter-particle interactions. An indication of the actual sharpness of the transition could be hypothesised by considering some of the inter-particle interactions. The scattering cross section of a plasmonic nanoparticle, such as these gold nanodisks, is significantly enhanced at the plasmon resonance, a value determined by both the material and shape of the particle. Should a second particle be in close proximity this resonance can be red-shifted, depending on the separation. Such an effect is well utilised through plasmon rulers [109]. For plasmon rulers a shift has been seen at gap sizes as large as 33 nm [110], showing that there must be some particle interaction during the transition. By considering the particle pair as a single scattering cross section it is expected to be the combination of a cross section σ_y for individual particles and the red-shifted cross section σ_x for the pair, as schematically depicted in Figure 6.7. The system employs

532 nm as its excitation wavelength so as to maximise the scattering from individual particles, this is therefore far from the resonance of the pair, decreasing this contribution of the interaction to the detected signal. It is expected that this σ_x scattering cross section is the cross section that corresponds to the $E_{0,x}$ component. The gap detection limit therefore depends on the ratio between σ_x and σ_y. Should $\sigma_x >> \sigma_y$, the scattering distribution will be saturated by the Gaussian $E_{0,x}$ component. Two factors are important to consider here. First that the resonance is shifted for σ_x so naturally will be smaller with increasing distance. Second, that the E_x component is ~16 times greater than $E_{0,y}$ so σ_x does not have to equal σ_y for both components to be balanced. Further work would focus on this transition area through fabricating a smaller gap size to fully measure the effect on the scattering signature, to see if this hypothesis is correct.

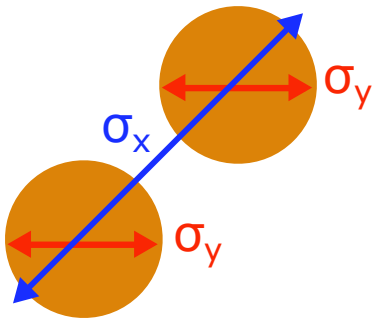

Figure 6.7: Schematic of splitting the particle pair into two different scattering cross sections. σ_y, the scattering cross section for the individual particles which results in the E_y contribution. Where σ_x is the scattering cross section of the pair and results in the additional E_x contribution.

Throughout this chapter the scattering signature from a pair of nanodisk structures, as their separation distance was systematically reduced, was investigated. It was found that as soon as the disks were in contact there was a significant difference in the produced scattering signature. This system could therefore be applied to the detection of nanogap sizes. Through investigating several pair situations it was found that at least a 20 nm gap size could be identified, far below the diffraction limit. It was discussed how the scattering signature pro-

duced from two close particles may be the same as that of two disks in contact; leading to the expected fundamental gap detection limit of this system.

Chapter 7

Anisotropic etching of gold crystals for plasmonic devices.

Plasmonic devices fabricated through techniques such as thermal evaporation have poor efficiency due to the loss arising from surface roughness. Crystalline gold has therefore drawn the attention of the plasmonic community as a more efficient alternative. Within this chapter a chlorine reactive ion etch is shown to anisotropically etch the crystal faces, presenting a method to create even smoother structures for higher efficiencies[1].

[1]This chapter contains datasets and analysis from a manuscript being prepared for submission

Quantum plasmonics, the combination of plasmonics and quantum photonics, is a field that could enable classical and quantum processing on small but complex circuits [111]. There are two main components that need to be addressed to achieve this goal: the material and fabrication of the plasmonic circuit; and the coupling of single photons into it. The use of quantum emitters, such as nitrogen-vacancy centres, in combination with plasmonic waveguides has been explored extensively as a means of coupling photons to the desired circuitry [112–114]. The inherent nature of surface plasmons significantly enhances light matter interactions [115], enabling very efficient coupling of quantum emitters [116].

The circuitry for processing applications need to have a well-defined geometry that can be fabricated with minimal imperfections [116]. Unfortunately, many of the fabrication methods used to create 2D metallic nanostructures result in some form of variation from the desired structure. For example, structures formed from evaporated metals present a surface roughness, due to their polycrystalline form, leading to propagation loss [117, 118]. The inefficient polycrystalline materials could be avoided by utilising chemically synthesising metallic nanowires [116]. While this approach highlights that larger propagation lengths can be obtained it cannot be easily used to manufacture complex circuitry.

Fortunately, chemically synthesised materials are not limited to wires alone. 2D single crystal gold flakes can be grown, with lateral dimensions of up to millimetres in size [119–121]. These large crystals provide the ideal target for top down fabrication processes; such as the widely used combination of electron-beam lithography and dry etching techniques [122, 123]. This processing and material combination provides an excellent platform for plasmonic circuitry, enabling both complex structures and enhancement from the crystalline material [124].

In this chapter a further improvement to the fabrication process is explored by

applying an anisotropic etch to form plasmonic structures. Due to their confinement, surface plasmons are sensitive to a substrates roughness. Anisotropic etching can enable smoother and therefore more efficient structures. Using this dry etch technique the feasibility to fabricate complex structures, such as a plasmonic interferometer, is explored.

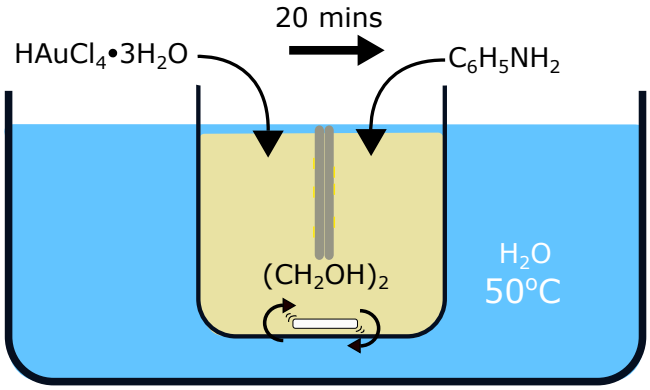

Figure 7.1: Schematic layout for the crystal growth reaction. Two substrates are suspended in $(CH_2OH)_2$ heated in a water bath. While stirring, $HAuCl_4 \cdot 3H_2O$ is added. After 20 minutes $C_6H_5NH_2$ is added.

The crystal growth method is based on a similar one prepared by Wu *et.al.* [119] and the schematic layout is depicted in Figure 7.1. Before growth a silicon substrate is cleaned through a 10 minute sonication with acetone, followed by a second 10 minutes with isopropanol and dried with a nitrogen spray gun. The substrates are then suspended vertically in 40 mL of ethylene glycol heated to 50 °C in a water bath as shown in Figure 7.1. The ethylene glycol is stirred at 200 rpm and 360 μL of 0.1 M gold (III) chloride trihydrate in ethylene glycol is added. After 20 minutes 360 μL of 0.1 M aniline within ethylene glycol is added and left for a further 5 minutes. The stirring is then stopped and kept in an enclosed water bath at 50 °C for 24 hours. The substrates are removed and sequentially washed with methanol and IPA under sonication for a further 5 minutes each. The resulting crystals can be seen in Figure 7.2 as imaged by optical microscopy. The preferential growth of the crystal results in the {111}

plane lying parallel to the image plane [124] on top of the {100} silicon plane. It should be noted that the orientation of the substrate with respect to the rotation of the stirrer bar has an affect on the concentration of crystals on the surface, with the side facing the flow generally having a greater number of crystals. To be able to etch structures into individual gold crystals a mask covering the full sample is required to enable all structures to be written in a single run in the Raith Voyager e-beam lithography system. This requires not only the location of the crystals, but also their orientation, so that the crystal face direction is known with respect to the written structure. The substrate is combined with fiducial grid markers so that the location and orientation can be determined, this allows each crystal to be assigned a tailored structure. The mask for an array of labelled grid markers was produced on the sample through photolithographic means. Markers were initially formed through the thermal evaporation of a Cr/Au layer, however the gold layer was found to react during the crystal growth, seen in Figure 7.2, and causes a significant reduction in the number of suitably sized crystals. For that reason all substrates containing fiducial markers were produced through etching of the silicon substrate, creating trenches and therefore preventing any reaction between the markers and growth solution.

After the growth stage the relative location of each gold crystal was identified with respect to the fiducial markers. The sample was subsequently coated in MaN, a negative e-beam resist, and exposed using a Raith Voyager e-beam lithography system. The sample was then etched using an inductively coupled plasma reactive ion etch (Oxford Instruments System 100 ICP 180) with the etch parameters stated in Table 7.1, based the work from Aydemir and Akin [125]. Here ICP power dictates the ion density whereas the RF power is used to accelerate the ions towards the surface. A 10 mTorr spike is used for initial plasma generation and tuning of the coils before dropping to 5 mTorr for the duration of the etch process.

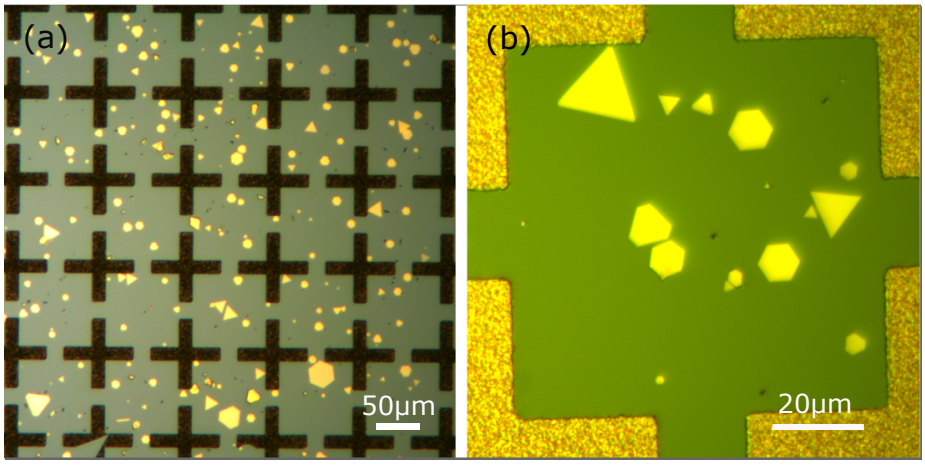

Figure 7.2: Typical optical images of the crystal structures after growth on a silicon substrate with gold grid markers. (a) and (b) present different scales representing the general concentration of crystals produced.

ICP Power	600 W
RF Power	250 W
Argon Flow Rate	5 sccm
Chlorine Flow Rate	15 sccm
Pressure	5 mTorr (10 mTorr Spike)
Temperature	40 °C

Table 7.1: Table of the ICP etch parameters for anisotropic etching of gold crystals

An etch time of 60 seconds was found to be the optimal in generating the test structures seen within this chapter. Higher durations generally resulted in the complete removal of the mask layer due to the non-specific etch characteristics of a Cl etch.

In attempting to fabricate a smooth structured sample of lettering it was observed that the resulting pattern would not follow the mask correctly. Instead of straight and smooth lines following the mask, jagged edges were formed, as shown in Figure 7.3(a) with the intended structure overlayed in Figure 7.3(b). Closer inspection of Figure 7.3(a) reveals that these jagged edges were orientated at multiples of 60° apart, indicating that they follow the crystal symmetry. To further investigate this effect specific masks were created, a single 1 μm circu-

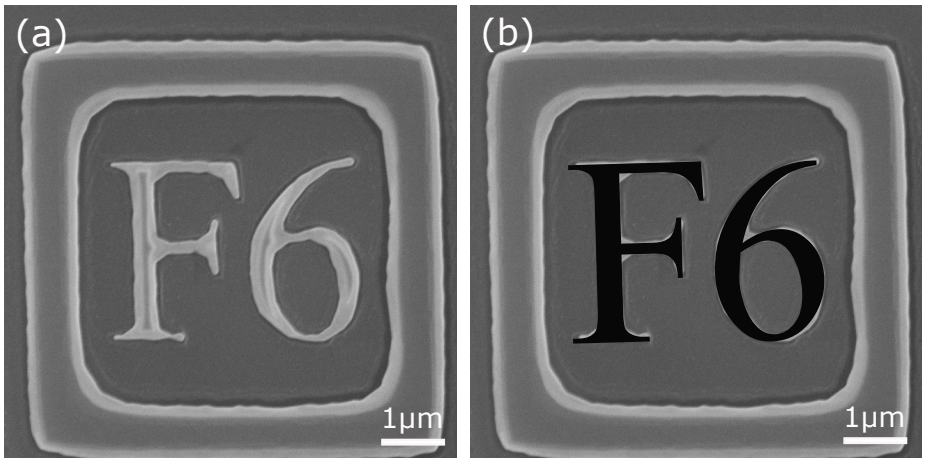

Figure 7.3: (a) SEM of the resulting structure after etching with (b) overlaying the intended mask structure.

lar hole and zig-zag lines, orientated both along the crystal faces and 30° from the faces. The results are shown in Figure 7.4. Figure 7.4(a) highlights with a red dotted line the mask pattern. Rather than etching in a uniform circle corresponding to the mask the crystal is etched quicker along set crystal faces, resulting in a hexagon etch pattern, seen in Figure 7.4 (c). This is further confirmed by the resulting structure from the mask seen in Figure 7.4(b), where the higher detail structure, that can also be seen in the non-crystal material in (d), is lost when the line is orientated along one of the crystal faces. The lines orientated along crystal faces are much smoother and do not show evidence of the initial zig-zag structure. Not all of the crystal in Figure 7.4(d) appears to be etched, this is suspected to be a result of the mask not being fully removed due to the close proximity of one of the fiducial markers. Failure to remove this mask not only protects the crystal from being etched but also causes the rough texturing that can be seen in the SEM image. These images show that just like there is a preferential growth direction of the crystals, there is a preferential etch direction when utilising this etch method.

The preferential etch directions can be exploited in unexpected ways when it comes to designing specific structures that have minimal losses. As seen in

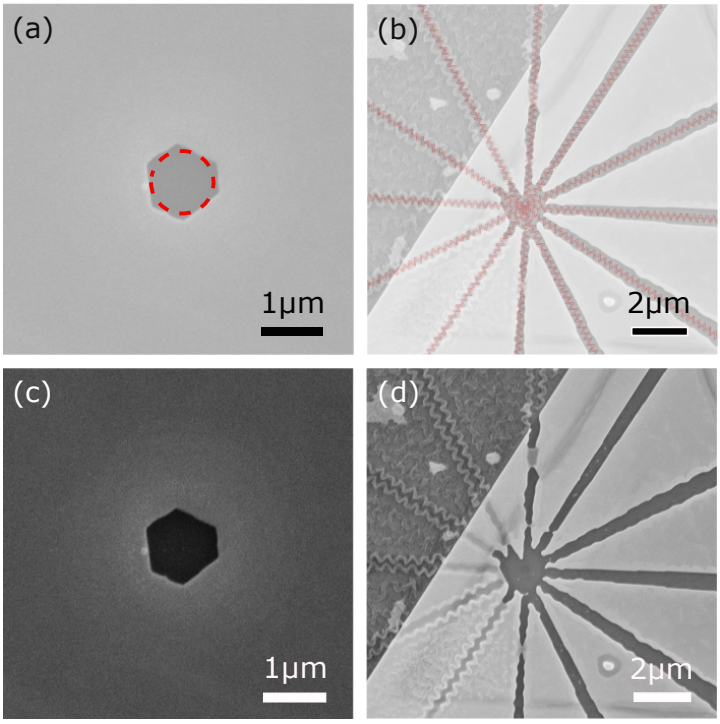

Figure 7.4: (a) and (b) show the hole and zig-zag mask, respectively. (c) and (d) depict the resulting etch from the hole and zig-zag mask, respectively.

Figure 7.4(d) detailed structures orientated incorrectly to the crystal faces are almost completely removed. Figure 7.5(a) shows how different design considerations can create a variety of structures. By aligning a number of 1 μm holes along a crystal face it can be seen how if left for longer etch time the resulting etch would have smooth side walls aligned with a crystal face. In the cases that the holes are not aligned correctly, it is clearly seen that zigzag lines are formed, posing a problem for some structures. If however structures and devices are designed with this in mind and the etch process is correctly controlled, then it should be possible to create very smooth edges following the crystal faces. An example of such a designed structure is shown in Figure 7.5, an interferometer, imaged with SEM (b) and AFM (c). By designing the structure so that edges only lie along the crystal face directions, fabrication not only becomes possible but should also result in smoother structures due to the preferential etch. Inspection of the AFM data reveals that the gold has been significantly

under etched leaving only a thin line on top of the interferometer arms which are primary silicon, highlighting that further work needs to be conducted to fully characterise the etch.

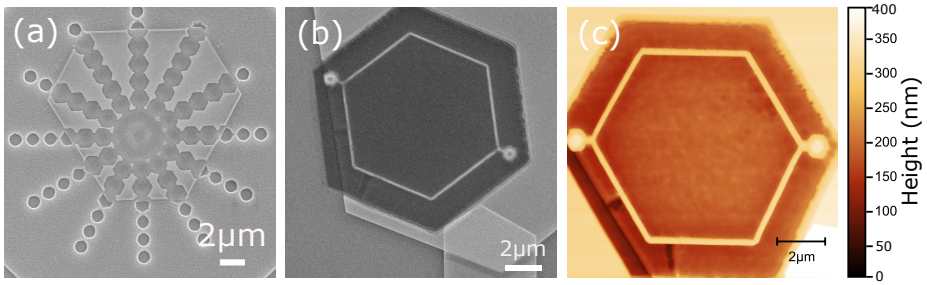

Figure 7.5: (a) Numerous 1 μm holes orientated along different angles with respect to the crystal faces. Example of a interferometer designed to utilise the etching preference of the method imaged by SEM (b) and AFM (c).

Throughout this chapter the fabrication of plasmonic devices from single crystalline materials using a chemical dry etching method was investigated. Dry etching through use of ICP results in an anisotropic etch potentially allowing the fabrication of smooth side walls in plasmonic structures, provided that the designs for devices carefully consider the etching face preference. This could enable a significant reduction in loss for plasmonic devices fabricated in this way. Further work would begin to investigate the etch parameters and how they can be controlled to optimise the structures created following this process.

Chapter 8

Conclusion and outlook.

The first section of this chapter presents the key messages from this thesis. The second section focuses on the outlook for further experiments related to the presented work.

8.1 Conclusion

Throughout this thesis the usage of interferometric cross polarised microscopy (ICPM) as a means of characterising plasmonic nanostructures was investigated. Initially the technique was applied to a bound fluorophore and plasmonic nanoparticle used as a probe for correlative light electron microscopy (CLEM). In this scheme the fluorophore is typically detected in wide field light microscopy. The sample can then be imaged with high resolution electron microscopy at the same location by identifying the detectable gold nanoparticles that are attached to the fluorophores. This relocation assumes that the fluorescent signal and nanoparticle are at the same location. Characterising this CLEM probe through ICPM reveals that this is not the case. By combining the ability of ICPM to detect the scattering signals from individual nanoparticles with an avalanche photodiode, the system is able to image both parts of the probe simultaneously. It was discovered that the close proximity of the plasmonic particle quenched the fluorescence by at least 95%. This poses a serious issue for the usage of such probes as their primary role to enable colocalisation cannot be achieved.

Chapters 3, 5 and 6 investigated how structural changes in a scattering particle will affect the spatial distribution of the detected scattering signal. Deviations from the expected spatial distribution have repeatedly been seen throughout previous experiments with ICPM. The work conducted in Chapter 3 revealed that these deviations arise due to the particles themselves rather than the imaging setup. It was determined that this influence is a result of the inherent dependence of ICPM on polarisation. Imaging an ideal point particle would produce a scattering distribution identical to the generated $E_{0,y}$ component in the focus of a high NA objective. The cross polarised nature of the system prevents any contribution from the $E_{0,x}$ and $E_{0,z}$ components. The ideal point particle does not exist in practice. These real particles will always have some

form of asymmetry, even if it is from the crystal structure of the nanoparticles. The asymmetric structure will then project the incident polarisation across the other axis, resulting in a contribution from the $E_{0,x}$ and $E_{0,z}$ spatial distributions in the detected signal. This behaviour not only affects ICPM but is also relevant to any modal dependent imaging such as spatial mode decomplexing (SPADE). This technique was utilised as a means of increasing the resolution of an optical system by analysing each individual spatial mode. As revealed throughout Chapter 3, attempts to conduct such measurements with high NA objectives where extra spatial modes will be generated will make decomplexing the signals significantly more difficult.

The contribution of these extra modes was investigated more rigorously in Chapter 5 where large arrays of nanostructures with defined orientations and aspect ratios were investigated. A theoretical model based on polarisation projection between two crossed polarisers and the electrostatic polarisability was developed to describe the observed behaviour for the 2D situation. A strong correlation between the predicted spatial distribution and those detected was found. There were however deviations in the magnitude of the signal across multiple nanostructures. This irregularity was attributed to imperfect nanofabrication resulting in less well defined structures as confirmed by AFM imaging. By utilising the theoretical model and spatial structure of the $E_{0,y}$ mode, a method of determining the full 2D orientation of individual nanorods was presented. Inspection of the theoretical description suggests the ability to identify both orientation and aspect ratio provided they can be adequately decoupled from each other.

The transition point for the scattering signature between an asymmetric particle and real point particle was of interest in Chapter 6. Here the scattering signature arising from a pair of nanodisks with decreasing separation at multiple orientations was investigated. When the pair were orientated parallel to the incident polarisation the system behaved in an expected fashion. The $E_{0,y}$

scattering distribution for each disk moved closer together and merged until they were indistinguishable. Of much greater interest was the instance where the pair were separated at 45° to the incident polarisation. As identified from the previous chapters this orientation for asymmetric particles would result in the $E_{0,x}$ component being projected and detected. As seen from the theory presented in Chapter 5 this contribution is proportional to the aspect ratio of the particle. It was observed that when the two disks made contact to form a single rod, the scattered distribution changed significantly. By investigating this transition point, it was determined that a gap size as small as 20 nm could be detected. There is strong potential that this is not the limit and that the change in signature during this transition could be used to measure much smaller gap sizes.

Finally a fabrication method was presented that enables anisotropic etching of gold crystals. The ability to anisotropically etch a material is usually reserved for wet etching techniques, which are often difficult to control as a result of the liquid etchant. It was found that through use of a chlorine plasma anisotropic etching can be achieved using a dry etching technique. The ability to anisotropically etch a material such as gold crystals has great promise for the fabrication of plasmonic circuitry, where surface roughness is a key contributor to loss. Gold crystalline material combined with an etch that follows the crystal faces to create smooth side walls provides an ideal platform to develop plasmonic devices.

8.2 Outlook

8.2.1 CLEM Probe Variation

The results in Chapter 2 would indicate that the example probe is unsuitable for use as a marker. The method of conjugating a fluorophore with gold nanoparticles however may still have value. The distance between the two entities, a quantity unknown for the tested probe, has a large effect on the quenching ef-

ficiency [126]. Increasing the separation through design of further probes may alleviate such problems. Further to this, the size of the gold nanoparticle is also a consideration into quenching effects. The 10 nm probe used within this investigation is considered large for many applications given how the size can affect cellular uptake, a more common gold probe size is 1.4 nm. This drastic decrease in size from the probe tested in Chapter 2 could result in a different quenching efficiency [126] and may make it possible for such probes to be used. The very small size of the scattering particle would put it outside the sensitivity range of our current ICPM system. To combat this a future study that correlates the fluorescence of individual CLEM probes with AFM data would allow for a characterisation of these smaller probes. Such correlation can easily be achieved through fabricated alignment markers, such as a grid on a mica surface, combined with wide field imaging for relocation as is utilised in Chapter 3.

8.2.2 Reflection Based ICPM with a 1.45 NA Objective

The data for Chapter 4 was collected using a 0.9 NA objective. The ultimate aim is to use a 1.45 NA objective. To date the use of the 1.45 NA objective was unsuccessful as it is difficult to obtain and maintain cancellation. Upon alignment of the 0.9 NA objective in reflection with no object in the focus, it is possible to cross the polarisation states of the reference and signal branch so that no background signal is detected. With the 1.45 NA objective this cancellation is not possible suggesting that the reflected spot does not contain one single polarisation state. The difference between the functioning 0.9 NA and 1.45 NA is that the latter will collect light from beyond the critical angle. It is suspected that this contribution alters the state of the reflected light. To test this glycerol ($n = 1.474$) was applied to the surface of the transparent sample ($n = 1.515$). The refractive index difference pushes the critical angle outside the collection range of the 1.45 NA objective. This enabled the reflected signal to be cancelled with the reference beam, though at the expense of signal strength.

Cancellation can also be achieved by a reduction of the effective NA through reduction of the beam width.

Further work is required to understand how the reflected beam is affected outside the critical angle and why severe instability is observed when cancelling using an NA of 1.45. Simulating the scheme with a finite difference time domain approach, such as the Angora [127] or MEEP [128] packages, would enable a greater understanding of the transformation and possible ways to overcome the issue. Investigating the difference between the signal to noise ratio for the 0.9 NA and the 1.45 NA with the additional glycerol also requires further study to see if any enhancement can be gained.

8.2.3 The Limits of Gap Size Detection

The work in Chapter 6 highlighted the sharp transition when two scattering objects come into contact. While a brief attempt at explaining the transition area was discussed it was not possible to confidently state the fundamental limit of this gap detection technique. Simulation of the situation through a finite difference time domain method to determine the distance at which the coupling between the two would influence the scattering is one approach. The other would be to experimentally image samples with much smaller separation distances so as to fill the transition zone in Figure 6.6. This could be achievable though nanofabrication as presented within Chapter 6 however the small separation distances would make fabrication challenging. A more practical approach may be to chemically bind nanoparticles together, such as with defined length oligonucleotides, or by laying a transparent polymer on top of a thin gold film then depositing gold nanoparticles on top. This approach would induce a $E_{0,z}$ contribution as opposed to the $E_{0,x}$. The lower magnitude of the $E_{0,z}$ component compared to that of the $E_{0,x}$ may also result in a change in the detection limits leading to different sensitivities along different axis.

8.2.4 Towards 3D Orientation Detection

A technique to determine the 3D orientation of individual particles is put forward in Chapter 5. While the theory and presented simulations matched well with the experimental data, a determination of the unknown orientation of nanorod was not achieved. This was partly due to poor fabrication quality. The need to fabricate samples could be removed by depositing gold nanorods on a gridded coverslip. Using the grid as a fiducial marker, in a similar way to in Chapter 3, the optical image could be correlated to AFM images or even SEM given the newly constructed reflection modality. Testing a 3D sample would be a much more difficult task given the requirement for the structure of interest to remain stationary during imaging.

8.2.5 Gold Crystals

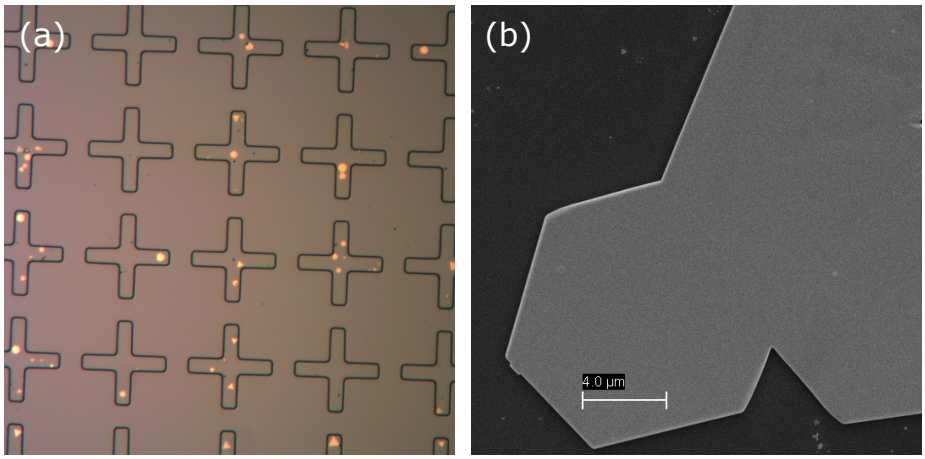

Figure 8.1: (a) Specific location growth of crystals and (b) potential of growing large sheets

Chapter 7 describes a method for anisotropic etching of gold crystals. These gold crystals are of great interest to creating plasmonic circuitry however one consideration which was not addressed is the working area. Currently the size of the crystals is limited, in turn limiting the complexity of plasmonic devices and structures. Figure 8.1(a) shows evidence that the location of crystal growth can

be controlled to some degree. Upon using a photo resist to create the gridded structure seen here not all of the residual photoresist was removed after the etching process. The remaining thin layer of photoresist prevented any growth in this area and instead concentrated the crystal growth in the gridded patterns. Evidence was also seen that if correctly orientated the individual crystals can grow together, seen in Figure 8.1(b). If the seeds for crystal growth were controllably deposited onto the substrate surface in a dense array and the mask removed to allow further growth a larger surface area could be fabricated. While the structure and plasmonic properties of this interface between the two crystals needs further study it may provide a promising method for large crystalline gold plasmonic devices.

Bibliography

[1] D. J. Stephens, "Light microscopy techniques for live cell imaging," *Science*, vol. 300, no. 5616, pp. 82–86, 2003.

[2] K. Bahlmann, S. Jakobs, and S. W. Hell, "4pi-confocal microscopy of live cells," *Ultramicroscopy*, vol. 87(3), pp. 155–164, 2001.

[3] T. A. Planchon, L. Gao, D. E. Milkie, M. W. Davidson, J. A. Galbraith, C. G. Galbraith, and E. Betzig, "Rapid three-dimensional isotropic imaging of living cells using Bessel beam plane illumination," *Nature Methods*, vol. 8, no. 5, pp. 417–423, 2011.

[4] J. Rao, A. Dragulescu-Andrasi, and H. Yao, "Fluorescence imaging in vivo: recent advances," *Current Opinion in Biotechnology*, vol. 18, no. 1, pp. 17–25, 2007.

[5] S. Kumar, N. Harrison, R. Richards-Kortum, and K. Sokolov, "Plasmonic nanosensors for imaging intracellular biomarkers in live cells," *Nano Letters*, vol. 7, no. 5, pp. 1338–1343, 2007.

[6] A. Miyawaki, A. Sawano, and T. Kogure, "Lighting up cells: labelling proteins with fluorophores," *Nature Cell Biology*, p. 7, 2003.

[7] E. Kim and S. B. Park, "Chemistry as a prism: a review of light-emitting materials having tunable emission wavelengths," *Chemistry - An Asian Journal*, vol. 4, no. 11, pp. 1646–1658, 2009.

[8] F. Helmchen and W. Denk, "Deep tissue two-photon microscopy," *Nature Methods*, vol. 2, no. 12, pp. 932–940, 2005.

[9] J. P. Hoogenboom, J. Hernando, E. M. H. P. van Dijk, N. F. van Hulst, and M. F. García-Parajó, "Power-law blinking in the fluorescence of single organic molecules," *ChemPhysChem*, vol. 8, no. 6, pp. 823–833, 2007.

[10] X. Michalet, "Quantum dots for live cells, in vivo imaging, and diagnostics," *Science*, vol. 307, no. 5709, pp. 538–544, 2005.

[11] J. K. Jaiswal, E. R. Goldman, H. Mattoussi, and S. M. Simon, "Use of quantum dots for live cell imaging," *Nature Methods*, vol. 1, no. 1, pp. 73–78, 2004.

[12] T. Jamieson, R. Bakhshi, D. Petrova, R. Pocock, M. Imani, and A. M. Seifalian, "Biological applications of quantum dots," *Biomaterials*, vol. 28, no. 31, pp. 4717–4732, 2007.

[13] A. M. Derfus, W. C. W. Chan, and S. N. Bhatia, "Probing the cytotoxicity of semiconductor quantum dots," *Nano Letters*, vol. 4, no. 1, pp. 11–18, 2004.

[14] N. Mohan, C.-S. Chen, H.-H. Hsieh, Y.-C. Wu, and H.-C. Chang, "In vivo imaging and toxicity assessments of fluorescent nanodiamonds in *Caenorhabditis elegans*," *Nano Letters*, vol. 10, no. 9, pp. 3692–3699, 2010.

[15] O. Faklaris, D. Garrot, V. Joshi, F. Druon, J.-P. Boudou, T. Sauvage, P. Georges, P. A. Curmi, and F. Treussart, "Detection of single photoluminescent diamond nanoparticles in cells and study of the internalization pathway," *Small*, vol. 4, no. 12, pp. 2236–2239, 2008.

[16] S. Hohng and T. Ha, "Near-complete suppression of quantum dot blinking in ambient conditions," *Journal of the American Chemical Society*, vol. 126, no. 5, pp. 1324–1325, 2004.

[17] B. Mahler, P. Spinicelli, S. Buil, X. Quelin, J.-P. Hermier, and B. Dubertret, "Towards non-blinking colloidal quantum dots," *Nature Materials*, vol. 7, no. 8, pp. 659–664, 2008.

[18] B. T. Miles, A. B. Greenwood, B. R. Patton, and H. Gersen, "All-optical method for characterizing individual fluorescent nanodiamonds," *ACS Photonics*, vol. 3, no. 3, pp. 343–348, 2016.

[19] N. G. Khlebtsov and L. A. Dykman, "Optical properties and biomedical applications of plasmonic nanoparticles," *Journal of Quantitative Spectroscopy and Radiative Transfer*, vol. 111, no. 1, pp. 1–35, 2010.

[20] S. Eustis and M. A. El-Sayed, "Why gold nanoparticles are more precious than pretty gold: noble metal surface plasmon resonance and its enhancement of the radiative and nonradiative properties of nanocrystals of different shapes," *Chemical Society Reviews*, vol. 35, no. 3, pp. 209–217, 2006.

[21] V. Amendola, R. Pilot, M. Frasconi, O. M. Maragò, and M. A. Iatì, "Surface plasmon resonance in gold nanoparticles: a review," *Journal of Physics: Condensed Matter*, vol. 29, no. 20, p. 203002, 2017.

[22] X. Huang, P. K. Jain, I. H. El-Sayed, and M. A. El-Sayed, "Plasmonic photothermal therapy (PPTT) using gold nanoparticles," *Lasers in Medical Science*, vol. 23, no. 3, pp. 217–228, 2008.

[23] M. Liu, J. Chao, S. Deng, K. Wang, K. Li, and C. Fan, "Dark-field microscopy in imaging of plasmon resonant nanoparticles," *Colloids and Surfaces B: Biointerfaces*, vol. 124, pp. 111–117, 2014.

[24] P. Zijlstra and M. Orrit, "Single metal nanoparticles: optical detection, spectroscopy and applications," *Reports on Progress in Physics*, vol. 74, no. 10, p. 106401, 2011.

[25] L. Xiao, Y. Qiao, Y. He, and E. S. Yeung, "Three dimensional orientational imaging of nanoparticles with darkfield microscopy," *Analytical Chemistry*, vol. 82, no. 12, pp. 5268–5274, 2010.

[26] C. Leduc, J.-M. Jung, R. R. Carney, F. Stellacci, and B. Lounis, "Direct investigation of intracellular presence of gold nanoparticles *via* photothermal heterodyne imaging," *ACS Nano*, vol. 5, no. 4, pp. 2587–2592, 2011.

[27] S. Berciaud, D. Lasne, G. A. Blab, L. Cognet, and B. Lounis, "Photothermal heterodyne imaging of individual metallic nanoparticles: Theory versus experiment," *Physical Review B*, vol. 73, no. 4, p. 045424, 2006.

[28] L. Tong, Q. Wei, A. Wei, and J.-X. Cheng, "Gold nanorods as contrast agents for biological imaging: optical properties, surface conjugation and photothermal effects," *Photochemistry and Photobiology*, vol. 85, no. 1, pp. 21–32, 2009.

[29] A. Gaiduk, M. Yorulmaz, P. V. Ruijgrok, and M. Orrit, "Room-temperature detection of a single molecule's absorption by photothermal contrast," *Science*, vol. 330, no. 6002, pp. 353–356, 2010.

[30] B. Deutsch, R. Beams, and L. Novotny, "Nanoparticle detection using dual-phase interferometry," *Applied Optics*, vol. 49, pp. 4921–4925, 2010.

[31] O. Avci, N. Ünlü, A. Özkumur, and M. Ünlü, "Interferometric reflectance imaging sensor (IRIS)—A platform technology for multiplexed diagnostics and digital detection," *Sensors*, vol. 15, no. 7, pp. 17649–17665, 2015.

[32] J. Ortega-Arroyo and P. Kukura, "Interferometric scattering microscopy (iSCAT): new frontiers in ultrafast and ultrasensitive optical microscopy," *Physical Chemistry Chemical Physics*, vol. 14, no. 45, p. 15625, 2012.

[33] D. Cole, G. Young, A. Weigel, A. Sebesta, and P. Kukura, "Label-free single-molecule imaging with numerical-aperture-shaped interferometric scattering microscopy," *ACS Photonics*, vol. 4, no. 2, pp. 211–216, 2017.

[34] J. Ortega Arroyo, J. Andrecka, K. M. Spillane, N. Billington, Y. Takagi, J. R. Sellers, and P. Kukura, "Label-free, all-optical detection, imaging, and tracking of a single protein," *Nano Letters*, vol. 14, no. 4, pp. 2065–2070, 2014.

[35] M. Liebel, J. T. Hugall, and N. F. van Hulst, "Ultrasensitive label-free nanosensing and high-speed tracking of single proteins," *Nano Letters*, vol. 17, no. 2, pp. 1277–1281, 2017.

[36] F. Masia, W. Langbein, P. Watson, and P. Borri, "Resonant four-wave mixing of gold nanoparticles for three-dimensional cell microscopy," *Optics Letters*, vol. 34, no. 12, p. 1816, 2009.

[37] G. Zoriniants, F. Masia, N. Giannakopoulou, W. Langbein, and P. Borri, "Background-free 3d nanometric localisation and sub-nm asymmetry detection of single plasmonic nanoparticles by four-wave mixing interferometry with optical vortices," *Physical Review X*, vol. 7, no. 4, 2017. arXiv: 1707.04888.

[38] R. Stierlin, R. Bättig, P. D. Henchoz, and H. P. Weber, "Excess-noise suppression in a fibre-optic balanced heterodyne detection system," *Optical and Quantum Electronics*, vol. 18, no. 6, pp. 445–454, 1986.

[39] M. Celebrano, P. Kukura, A. Renn, and V. Sandoghdar, "Single-molecule imaging by optical absorption," *Nature Photonics*, vol. 5, no. 2, pp. 95–98, 2011.

[40] F. V. Ignatovich and L. Novotny, "Real-time and background-free detection of nanoscale particles," *Physical Review Letters*, vol. 96, no. 1, 2006.

[41] M. Tsang, R. Nair, and X.-M. Lu, "Quantum theory of superresolution for two incoherent optical point sources," *Physical Review X*, vol. 6, no. 3, 2016. arXiv: 1511.00552.

[42] B. T. Miles, A. B. Greenwood, D. Benito-Alifonso, H. Tanner, M. C. Galan, P. Verkade, and H. Gersen, "Direct evidence of lack of colocalisation of fluorescently labelled gold labels used in correlative light electron microscopy," *Scientific Reports*, vol. 7, no. 1, p. 44666, 2017.

[43] E. Brown and P. Verkade, "The use of markers for correlative light electron microscopy," *Protoplasma*, vol. 244, no. 1-4, pp. 91–97, 2010.

[44] J. R. van Weering, E. Brown, T. H. Sharp, J. Mantell, P. J. Cullen, and P. Verkade, "Intracellular membrane traffic at high resolution," *Methods Cell Biol.*, vol. 96, pp. 619–648, 2010.

[45] P. de Boer, J. P. Hoogenboom, and B. N. G. Giepmans, "Correlated light and electron microscopy: ultrastructure lights up!," *Nature Methods*, vol. 12, no. 6, pp. 503–513, 2015.

[46] E. Dulkeith, A. C. Morteani, T. Niedereichholz, T. A. Klar, J. Feldmann, S. A. Levi, F. C. J. M. van Veggel, D. N. Reinhoudt, M. Möller, and D. I. Gittins, "Fluorescence quenching of dye molecules near gold nanoparticles: radiative and nonradiative effects," *Physical Review Letters*, vol. 89, no. 20, 2002.

[47] I. K. Kandela, R. Bleher, and R. M. Albrecht, "Multiple correlative immunolabeling for light and electron microscopy using fluorophores and colloidal metal particles," *Journal of Histochemistry & Cytochemistry*, vol. 55, no. 10, pp. 983–990, 2007.

[48] P. Anger, P. Bharadwaj, and L. Novotny, "Enhancement and quenching of single-molecule fluorescence," *Physical Review Letters*, vol. 96, no. 11, 2006.

[49] T. L. Jennings, M. P. Singh, and G. F. Strouse, "Fluorescent lifetime quenching near $d = 1.5$ nm gold nanoparticles: probing nset validity," *Journal of the American Chemical Society*, vol. 128, no. 16, pp. 5462–5467, 2006.

[50] S. A. Mutch, B. S. Fujimoto, C. L. Kuyper, J. S. Kuo, S. M. Bajjalieh, and D. T. Chiu, "Deconvolving single-molecule intensity distributions for quantitative microscopy measurements," *Biophysical Journal*, vol. 92, no. 8, pp. 2926–2943, 2007.

[51] S. Kawata, Y. Inouye, and P. Verma, "Plasmonics for near-field nano-imaging and superlensing," *Nature Photonics*, vol. 3, no. 7, pp. 388–394, 2009.

[52] S.-W. Chu, T.-Y. Su, R. Oketani, Y.-T. Huang, H.-Y. Wu, Y. Yonemaru, M. Yamanaka, H. Lee, G.-Y. Zhuo, M.-Y. Lee, S. Kawata, and K. Fujita, "Measurement of a saturated emission of optical radiation from gold nanoparticles: application to an ultrahigh resolution microscope," *Physical Review Letters*, vol. 112, no. 1, p. 017402, 2014.

[53] H.-Y. Wu, Y.-T. Huang, P.-T. Shen, H. Lee, R. Oketani, Y. Yonemaru, M. Yamanaka, S. Shoji, K.-H. Lin, C.-W. Chang, S. Kawata, K. Fujita, and S.-W. Chu, "Ultrasmall all-optical plasmonic switch and its application to superresolution imaging," *Scientific Reports*, vol. 6, no. 1, p. 24293, 2016.

[54] E. Wegel, A. Göhler, B. C. Lagerholm, A. Wainman, S. Uphoff, R. Kaufmann, and I. M. Dobbie, "Imaging cellular structures in super-resolution with SIM, STED and localisation microscopy: a practical comparison," *Scientific Reports*, vol. 6, no. 1, p. 27290, 2016.

[55] M. Fernández-Suárez and A. Y. Ting, "Fluorescent probes for super-resolution imaging in living cells," *Nature Reviews Molecular Cell Biology*, vol. 9, no. 12, pp. 929–943, 2008.

[56] B. Huang, H. Babcock, and X. Zhuang, "Breaking the diffraction barrier: super-resolution imaging of cells," *Cell*, vol. 143, no. 7, pp. 1047–1058, 2010.

[57] M. G. L. Gustafsson, "Nonlinear structured-illumination microscopy: wide-field fluorescence imaging with theoretically unlimited resolution," *Proceedings of the National Academy of Sciences*, vol. 102, no. 37, pp. 13081–13086, 2005.

[58] S. Chowdhury, A.-H. Dhalla, and J. Izatt, "Structured oblique illumination microscopy for enhanced resolution imaging of non-fluorescent, coherently scattering samples," *Biomedical Optics Express*, vol. 3, no. 8, p. 1841, 2012.

[59] F. Yang, A. Tashchilina, E. S. Moiseev, C. Simon, and A. I. Lvovsky, "Far-field linear optical superresolution via heterodyne detection in a higher-order local oscillator mode," *Optica*, vol. 3, no. 10, p. 1148, 2016.

[60] W.-K. Tham, H. Ferretti, and A. M. Steinberg, "Beating rayleigh's curse by imaging using phase information," *Physical Review Letters*, vol. 118, no. 7, p. 070801, 2017.

[61] M. Paúr, B. Stoklasa, Z. Hradil, L. L. Sánchez-Soto, and J. Rehacek, "Achieving the ultimate optical resolution," *Optica*, vol. 3, no. 10, p. 1144, 2016.

[62] B. Richards and E. Wolf, "Electromagnetic diffraction in optical systems. II. structure of the image field in an aplanatic system," *Proceedings of the Royal Society A: Mathematical, Physical and Engineering Sciences*, vol. 253, no. 1274, pp. 358–379, 1959.

[63] B. T. Miles, X. Hong, and H. Gersen, "On the complex point spread function in interferometric cross-polarisation microscopy," *Optics Express*, vol. 23, no. 2, p. 1232, 2015.

[64] L. Novotny and B. Hecht, *Principles of Nano-Optics*. Cambridge University Press, 2nd edition ed., 2012.

[65] L. M. Payne, W. Langbein, and P. Borri, "Polarization-resolved extinction and scattering cross-sections of individual gold nanoparticles measured by wide-field microscopy on a large ensemble," *Applied Physics Letters*, vol. 102, no. 13, p. 131107, 2013.

[66] Veerman, Garcia-Parajo, Kuipers, and Van Hulst, "Single molecule mapping of the optical field distribution of probes for near-field microscopy," *Journal of Microscopy*, vol. 194, no. 2-3, pp. 477–482, 1999.

[67] A. Freise and K. Strain, "Interferometer techniques for gravitational-wave detection," *Living Reviews in Relativity*, vol. 13, p. 1, 2010.

[68] F. Roddier, "Interferometric imaging in optical astronomy," *Physics Reports*, vol. 170, pp. 97–166, 1988.

[69] G. Rajshekhar, B. Bhaduri, C. Edwards, R. Zhou, L. L. Goddard, and G. Popescu, "Nanoscale topography and spatial light modulator characterization using wide-field quantitative phase imaging," *Optics Express*, vol. 22, no. 3, p. 3432, 2014.

[70] C. O Mahony, M. Hill, M. Brunet, R. Duane, and A. Mathewson, "Characterization of micromechanical structures using white-light interferometry," *Measurement Science and Technology*, vol. 14, no. 10, pp. 1807–1814, 2003.

[71] P. Marquet, B. Rappaz, P. J. Magistretti, E. Cuche, Y. Emery, T. Colomb, and C. Depeursinge, "Digital holographic microscopy: a noninvasive contrast imaging technique allowing quantitative visualization of living cells with subwavelength axial accuracy," *Optics Letters*, vol. 30, no. 5, p. 468, 2005.

[72] Y. Park, C. Depeursinge, and G. Popescu, "Quantitative phase imaging in biomedicine," *Nature Photonics*, vol. 12, no. 10, pp. 578–589, 2018.

[73] N. N. Boustany, S. A. Boppart, and V. Backman, "Microscopic imaging and spectroscopy with scattered light," *Annual Review of Biomedical Engineering*, vol. 12, no. 1, pp. 285–314, 2010.

[74] P. Török, P. Higdon, and T. Wilson, "On the general properties of polarised light conventional and confocal microscopes," *Optics Communications*, vol. 148, no. 4-6, pp. 300–315, 1998.

[75] T. Wilson and J. B. Tan, "Finite sized coherent and incoherent detectors in confocal microscopy," *Journal of Microscopy*, vol. 182, pp. 61–66, 1995.

[76] J. Pawley, *Handbook of confocal microscopy*. Springer, 3rd ed., 2006.

[77] E. C. Robinson, "Towards broadband optical spectroscopy of single nanostructures," *University of Bristol Thesis*, p. 156, 2013.

[78] F. Hooge, "1/f noise sources," *IEEE Transactions on Electron Devices*, vol. 41, no. 11, pp. 1926–1935, 1994.

[79] B. T. Miles, E. C. Robinson, E. M. H. P. van Dijk, I. D. Lindsay, N. F. van Hulst, and H. Gersen, "Sensitivity of interferometric cross-polarization microscopy for nanoparticle detection in the near-infrared," *ACS Photonics*, vol. 2, no. 12, pp. 1705–1711, 2015.

[80] T. Nishizaka, K. Oiwa, H. Noji, S. Kimura, E. Muneyuki, M. Yoshida, and K. Kinosita, "Chemomechanical coupling in F1-ATPase revealed by simultaneous observation of nucleotide kinetics and rotation," *Nature Structural & Molecular Biology*, vol. 11, no. 2, pp. 142–148, 2004.

[81] T. Ha, A. Y. Ting, J. Liang, W. B. Caldwell, A. A. Deniz, D. S. Chemla, P. G. Schultz, and S. Weiss, "Single-molecule fluorescence spectroscopy of enzyme conformational dynamics and cleavage mechanism," *Proceedings of the National Academy of Sciences*, vol. 96, no. 3, pp. 893–898, 1999.

[82] R. D. Vale, "The way things move: looking under the hood of molecular motor proteins," *Science*, vol. 288, no. 5463, pp. 88–95, 2000.

[83] J. Enderlein, E. Toprak, and P. R. Selvin, "Polarization effect on position accuracy of fluorophore localization," *Optics Express*, vol. 14, no. 18, p. 8111, 2006.

[84] D. M. Jameson and J. A. Ross, "Fluorescence polarization/anisotropy in diagnostics and imaging," *Chemical Reviews*, vol. 110, no. 5, pp. 2685–2708, 2010.

[85] T. Ha, T. Enderle, D. S. Chemla, P. R. Selvin, and S. Weiss, "Single molecule dynamics studied by polarization modulation," *Physical Review Letters*, vol. 77, no. 19, pp. 3979–3982, 1996.

[86] W. E. Moerner and D. P. Fromm, "Methods of single-molecule fluorescence spectroscopy and microscopy," *Review of Scientific Instruments*, vol. 74, no. 8, pp. 3597–3619, 2003.

[87] P. K. Jain, K. S. Lee, I. H. El-Sayed, and M. A. El-Sayed, "Calculated absorption and scattering properties of gold nanoparticles of different size, shape, and composition: applications in biological imaging and biomedicine," *The Journal of Physical Chemistry B*, vol. 110, no. 14, pp. 7238–7248, 2006.

[88] A. M. Alkilany and C. J. Murphy, "Toxicity and cellular uptake of gold nanoparticles: what we have learned so far?," *Journal of Nanoparticle Research*, vol. 12, no. 7, pp. 2313–2333, 2010.

[89] C. J. Murphy, A. M. Gole, J. W. Stone, P. N. Sisco, A. M. Alkilany, E. C. Goldsmith, and S. C. Baxter, "Gold nanoparticles in biology: beyond toxicity to cellular imaging," *Accounts of Chemical Research*, vol. 41, no. 12, pp. 1721–1730, 2008.

[90] L. Novotny, M. R. Beversluis, K. S. Youngworth, and T. G. Brown, "Longitudinal field modes probed by single molecules," *Physical Review Letters*, vol. 86, no. 23, pp. 5251–5254, 2001.

[91] L. Shang, K. Nienhaus, and G. Nienhaus, "Engineered nanoparticles interacting with cells: size matters," *Journal of Nanobiotechnology*, vol. 12, no. 1, p. 5, 2014.

[92] T. Li, Q. Li, Y. Xu, X.-J. Chen, Q.-F. Dai, H. Liu, S. Lan, S. Tie, and L.-J. Wu, "Three-dimensional orientation sensors by defocused imaging of gold nanorods through an ordinary wide-field microscope," *ACS Nano*, vol. 6, no. 2, pp. 1268–1277, 2012.

[93] T. ZüChner, A. V. Failla, A. Hartschuh, and A. J. Meixner, "A novel approach to detect and characterize the scattering patterns of single Au nanoparticles using confocal microscopy," *Journal of Microscopy*, vol. 229, no. 2, pp. 337–343, 2008.

[94] A. V. Failla, H. Qian, H. Qian, A. Hartschuh, and A. J. Meixner, "Orientational imaging of subwavelength au particles with higher order laser modes," *Nano Letters*, vol. 6, no. 7, pp. 1374–1378, 2006.

[95] W.-S. Chang, J. W. Ha, L. S. Slaughter, and S. Link, "Plasmonic nanorod absorbers as orientation sensors," *Proceedings of the National Academy of Sciences*, vol. 107, no. 7, pp. 2781–2786, 2010.

[96] X. Hong, E. M. P. H. van Dijk, S. R. Hall, J. B. Götte, N. F. van Hulst, and H. Gersen, "Background-free detection of single 5 nm nanoparticles through interferometric cross-polarization microscopy," *Nano Letters*, vol. 11, no. 2, pp. 541–547, 2011.

[97] L. M. Picco, L. Bozec, A. Ulcinas, D. J. Engledew, M. Antognozzi, M. A. Horton, and M. J. Miles, "Breaking the speed limit with atomic force microscopy," *Nanotechnology*, vol. 18, no. 4, p. 044030, 2007.

[98] B. Al-Qadi and T. Saiki, "Optical characterization and rotational dynamics observation of colloidal gold nanorods based on polarized light scattering microscopy," *Japanese Journal of Applied Physics*, vol. 49, no. 12, p. 125001, 2010.

[99] V. Myroshnychenko, J. Rodríguez-Fernández, I. Pastoriza-Santos, A. M. Funston, C. Novo, P. Mulvaney, L. M. Liz-Marzán, and F. J. García de Abajo, "Modelling the optical response of gold nanoparticles," *Chemical Society Reviews*, vol. 37, no. 9, p. 1792, 2008.

[100] C. Noguez, "Surface plasmons on metal nanoparticles: the influence of shape and physical environment," *The Journal of Physical Chemistry C*, vol. 111, no. 10, pp. 3806–3819, 2007.

[101] D.-K. Lim, K.-S. Jeon, H. M. Kim, J.-M. Nam, and Y. D. Suh, "Nanogap-engineerable Raman-active nanodumbbells for single-molecule detection," *Nature Materials*, vol. 9, no. 1, pp. 60–67, 2010.

[102] S. Kyu Kim, H. Cho, H.-J. Park, D. Kwon, J. Min Lee, and B. Hyun Chung, "Nanogap biosensors for electrical and label-free detection of biomolecular interactions," *Nanotechnology*, vol. 20, no. 45, p. 455502, 2009.

[103] C. Y. Lee, H. J. Park, J. Park, D. K. Park, H. Pyo, S. C. Kim, and W. S. Yun, "Quantification of antigen by digital domain analysis of integrated nanogap biosensors," *Biosensors and Bioelectronics*, vol. 97, pp. 273–277, 2017.

[104] T. Li, W. Hu, and D. Zhu, "Nanogap electrodes," *Advanced Materials*, vol. 22, no. 2, pp. 286–300, 2010.

[105] K. Ueno, S. Juodkazis, V. Mizeikis, K. Sasaki, and H. Misawa, "Clusters of closely spaced gold nanoparticles as a source of two-photon photoluminescence at visible wavelengths," *Advanced Materials*, vol. 20, no. 1, pp. 26–30, 2008.

[106] P. Z. El-Khoury, E. Khon, Y. Gong, A. G. Joly, P. Abellan, J. E. Evans, N. D. Browning, D. Hu, M. Zamkov, and W. P. Hess, "Electric field enhancement in a self-assembled 2d array of silver nanospheres," *The Journal of Chemical Physics*, vol. 141, no. 21, p. 214308, 2014.

[107] X. Chen, Z. Guo, G.-M. Yang, J. Li, M.-Q. Li, J.-H. Liu, and X.-J. Huang, "Electrical nanogap devices for biosensing," *Materials Today*, vol. 13, no. 11, pp. 28–41, 2010.

[108] C. Edwards, A. Arbabi, G. Popescu, and L. L. Goddard, "Optically monitoring and controlling nanoscale topography during semiconductor etching," *Light: Science & Applications*, vol. 1, no. 9, pp. e30–e30, 2012.

[109] C. Sönnichsen, B. M. Reinhard, J. Liphardt, and A. P. Alivisatos, "A molecular ruler based on plasmon coupling of single gold and silver nanoparticles," *Nature Biotechnology*, vol. 23, no. 6, pp. 741–745, 2005.

[110] B. M. Reinhard, M. Siu, H. Agarwal, A. P. Alivisatos, and J. Liphardt, "Calibration of dynamic molecular rulers based on plasmon coupling between gold nanoparticles," *Nano Letters*, vol. 5, no. 11, pp. 2246–2252, 2005.

[111] S. Bogdanov, M. Y. Shalaginov, A. Boltasseva, and V. M. Shalaev, "Material platforms for integrated quantum photonics," *Optical Materials Express*, vol. 7, no. 1, p. 111, 2017.

[112] E. Bermúdez-Ureña, C. Gonzalez-Ballestero, M. Geiselmann, R. Marty, I. P. Radko, T. Holmgaard, Y. Alaverdyan, E. Moreno, F. J. García-Vidal, S. I. Bozhevolnyi, and R. Quidant, "Coupling of individual quantum emitters to channel plasmons," *Nature Communications*, vol. 6, no. 1, p. 7883, 2015.

[113] A. Huck and U. L. Andersen, "Coupling single emitters to quantum plasmonic circuits," *Nanophotonics*, vol. 5, no. 3, pp. 483–496, 2016.

[114] H. Siampour, S. Kumar, and S. I. Bozhevolnyi, "Nanofabrication of plasmonic circuits containing single photon sources," *ACS Photonics*, vol. 4, no. 8, pp. 1879–1884, 2017.

[115] M. S. Tame, K. R. McEnery, S. K. Özdemir, J. Lee, S. A. Maier, and M. S. Kim, "Quantum plasmonics," *Nature Physics*, vol. 9, no. 6, pp. 329–340, 2013.

[116] H. Wei, D. Pan, S. Zhang, Z. Li, Q. Li, N. Liu, W. Wang, and H. Xu, "Plasmon waveguiding in nanowires," *Chemical Reviews*, vol. 118, no. 6, pp. 2882–2926, 2018.

[117] C.-Y. Wang, H.-Y. Chen, L. Sun, W.-L. Chen, Y.-M. Chang, H. Ahn, X. Li, and S. Gwo, "Giant colloidal silver crystals for low-loss linear and nonlinear plasmonics," *Nature Communications*, vol. 6, no. 1, p. 7734, 2015.

[118] P. Nagpal, N. C. Lindquist, S.-H. Oh, and D. J. Norris, "Ultrasmooth patterned metals for plasmonics and metamaterials," *Science*, vol. 325, no. 5940, pp. 594–597, 2009.

[119] X. Wu, R. Kullock, E. Krauss, and B. Hecht, "Single-crystalline gold microplates grown on substrates by solution-phase synthesis: Single-crystalline gold microplates grown on substrates by solution-phase synthesis," *Crystal Research and Technology*, vol. 50, no. 8, pp. 595–602, 2015.

[120] J. Zhou, A. Saha, J. Adamcik, H. Hu, Q. Kong, C. Li, and R. Mezzenga, "Macroscopic single-crystal gold microflakes and their devices," *Advanced Materials*, vol. 27, no. 11, pp. 1945–1950, 2015.

[121] T. Hartsfield, M. Gegg, P.-H. Su, M. R. Buck, J. A. Hollingsworth, C.-K. Shih, M. Richter, H. Htoon, and X. Li, "Semiconductor quantum dot lifetime near an atomically smooth Ag film exhibits a narrow distribution," *ACS Photonics*, vol. 3, no. 6, pp. 1085–1089, 2016.

[122] N. C. Lindquist, P. Nagpal, K. M. McPeak, D. J. Norris, and S.-H. Oh, "Engineering metallic nanostructures for plasmonics and nanophotonics," *Reports on Progress in Physics*, vol. 75, no. 3, p. 036501, 2012.

[123] T. A. Green, "Gold etching for microfabrication," *Gold Bulletin*, vol. 47, no. 3, pp. 205–216, 2014.

[124] R. Méjard, A. Verdy, O. Demichel, M. Petit, L. Markey, F. Herbst, R. Chassagnon, G. Colas-des Francs, B. Cluzel, and A. Bouhelier, "Advanced engineering of single-crystal gold nanoantennas," *Optical Materials Express*, vol. 7, no. 4, p. 1157, 2017.

[125] A. Aydemir and T. Akin, "Prevention of sidewall redeposition of etched byproducts in the dry Au etch process," *Journal of Micromechanics and Microengineering*, vol. 22, no. 7, p. 074004, 2012.

[126] M. Li, S. K. Cushing, Q. Wang, X. Shi, L. A. Hornak, Z. Hong, and N. Wu, "Size-dependent energy transfer between CdSe/ZnS quantum dots and gold nanoparticles," *The Journal of Physical Chemistry Letters*, vol. 2, no. 17, pp. 2125–2129, 2011.

[127] I. R. Capoglu, A. Taflove, and V. Backman, "Angora: a free software package for finite-difference time-domain electromagnetic simulation," *IEEE Antennas and Propagation Magazine*, vol. 55, no. 4, pp. 80–93, 2013.

[128] A. F. Oskooi, D. Roundy, M. Ibanescu, P. Bermel, J. Joannopoulos, and S. G. Johnson, "Meep: A flexible free-software package for electromagnetic simulations by the FDTD method," *Computer Physics Communications*, vol. 181, no. 3, pp. 687–702, 2010.